

A 3-D VIScous Vorticity Equation (VISVE) Method Applied to Flow Past a Hydrofoil of Elliptical Planform and a Propeller

Chunlin Wu, Spyros A. Kinnas

Ocean Engineering Group, Department of Civil, Architectural and Environmental Engineering
The University of Texas at Austin, Austin, Texas 78712, USA

ABSTRACT

A VIScous Vorticity Equation (VISVE) method that solves the vorticity equation is proposed in this paper to simulate the 3-D viscous flow past a hydrofoil or a propeller. The spatial concentration of vorticity leads to a local solver with a significantly small computational domain and a small number of cells, which results in much less computation time. The VISVE method is applied to a 3-D hydrofoil of elliptical planform. Calculated results provided good agreement with results from Navier-Stokes (N-S) methods, which validates the method. Also, some preliminary results of the flow past the 5-bladed NSRCD 4381 propeller are shown.

Keywords

Vorticity equation, 3-D hydrofoil, Propeller, Viscous flow.

1 INTRODUCTION

The 3-D vortex methods were successful in predicting the development of vortex in the absence of wall boundaries at high Reynolds numbers when the viscous effect is small. Generally, there are two types of mesh-free 3-D vortex methods, which are the vortex particle methods (Rehbach, 1978; Saffman, 1981) and the vortex filament methods (Chorin, 1981; Leonard, 1985). When meshes are partially used for solving the velocity, another type of 3-D vorticity method evolved from the above two methods. This method is known as the Vortex In Cell (VIC) method (Tryggvason et al., 1991; Almgren et al., 1994). For the above 3 methods, most of the existing literature neglect the effect of diffusion by assuming a high Reynolds number. Also, extensive studies have been conducted to include viscous corrections into those methods (Degond & Mas-Gallic, 1989; Leonard, 1980). Actually, the viscous diffusion affects the evolution of vortex significantly, especially at moderate and low Reynolds numbers. In addition, the viscosity is responsible for the production of vorticity on the wall. Therefore, the viscosity of fluids is essential in describing the interactions between fluid and solid near the wall surface.

When the full mesh is used, the method is usually referred to as the viscous vorticity method. Wu et al. (1995) proposed a 3-D vorticity method in Cartesian coordinates. The vorticity equation was discretized using the finite

difference method. Both the differential approach (Poisson's equation) and the integral approach (Biot-savart law) to recovering the solenoidal velocity field were studied. Hansen et al. (2003) solved the 3-D vorticity equation in the cylindrical coordinates. The vorticity equation was also discretized by using the finite difference method. A conjugate gradient method was adopted to solve the Poisson's equation. The method was applied to the translating flow and rotating flow in a pipe. Meitz and Fasel (2000) expanded the vorticity method into the Fourier space by the Fourier series to simulate the transitional and turbulent channel flow. Lo et al. (2005) applied the method to the 3-D lid-driven cavity flow at Reynolds numbers ranging from 100 to 2000.

For the existing applications of mesh-based 3-D vorticity methods, the computational domains are restricted to be quite simple since the boundary conditions contain mixed derivatives which are difficult to be implemented in general domains. In the proposed VISVE method, the 3-D vorticity equation is discretized in space by using the Finite Volume Method (FVM). A Poisson's equation is solved based on the finite volume discretization to recover the divergence-free velocity field. Moreover, a vorticity creation scheme is utilized to determine the amount of vorticity created by enforcing the no-slip and non-penetrating boundary conditions on the wall. The proposed vorticity creation scheme can treat the general domain boundaries, which significantly extends the scope of applications of the current method.

The VIScous Vorticity Equation (VISVE) method was first proposed by Tian & Kinnas (2015) as an alternative numerical tool to predict the performance of propeller at on- and off-design conditions. However, the method needs systematic validations and further improvements. Li & Kinnas (2017) applied the scheme to the unidirectional and alternating flows past a 2-D cylinder. Xing & Kinnas (2018) investigated the cavitating flow around a 2-D hydrofoil by including the mixture cavitation model into VISVE. Wu & Kinnas (2018) extended the VISVE method to 3-D hydrofoils considering the advection flow, in which only the advection and stretching terms were included in the vorticity equation. One year later, Wu & Kinnas (2019)

incorporated the diffusion term into the vorticity equation with skewness corrections and applied the improved scheme to fully viscous flow past a hydrofoil in non-orthogonal grids. Reliable results were obtained. The VISVE is also hybridly paralleled using both Open-MP and MPI to improve efficiency (Wu & Kinnas, 2018), where VISVE was shown to require significantly less computing time than N-S, due primarily to the significantly smaller grid in VISVE.

The VISVE method has several advantages in applying to simulate the flow past a propeller:

(a) It is a local solver with a significantly small computational domain and a small number of cells, which results in much less computation time.

(b) The effect of other blades is considered in an iterative manner, which is similar to the method used in PROPCAV and MPUF-3A. Only the flow on the key blade needs to be modeled. For axisymmetric case: duplicate the variables of the key blade. For non-axisymmetric case: use the variables of the key blade at different blade angles.

(c) The method allows for easily built grids. Since only the vicinity of the propeller needs to be modeled without using the periodic boundary conditions, the grid generation can be significantly simplified. Actually, this process can be made automated.

2 METHODOLOGY

2.1 Velocity Decomposition

The total velocity field \mathbf{v} is composed of two parts, which are the background flow velocity \mathbf{U}_{in} and the vorticity induced velocity \mathbf{u}

$$\mathbf{v} = \mathbf{U}_{in} + \mathbf{u} \quad (1)$$

For a given vorticity distribution, the corresponding velocity field can be uniquely determined according to the Helmholtz velocity decomposition. Therefore, the decomposition in Equation (1) is sole for a known flow field.

2.2 Vorticity Transport Equation

In the incompressible viscous flow, the Navier-Stokes (N-S) equation in the Eulerian frame reads

$$\frac{\partial \mathbf{v}}{\partial t} + (\mathbf{v} \cdot \nabla) \mathbf{v} = -\frac{\nabla p}{\rho} + \nu \nabla^2 \mathbf{v} \quad (2)$$

where \mathbf{v} represents the velocity vector, p is the pressure, t is the time, ρ is the density of the fluid and ν is the kinematic viscosity of the fluid. The vorticity transport equation could be obtained by taking curl on both sides of Equation (2), and the curl form of vorticity equation can be derived along the way as

$$\frac{\partial \boldsymbol{\omega}}{\partial t} + \nabla \times (\boldsymbol{\omega} \times \mathbf{q}) = -\nu \nabla \times (\nabla \times \boldsymbol{\omega}) \quad (3)$$

where $\boldsymbol{\omega} = \nabla \times \mathbf{v}$ is the vorticity. The biggest advantage of the curl formulation of the vorticity equation is that the divergence-free condition of vorticity is automatically satisfied in time. Equation (3) is discretized using the Finite Volume Method (FVM) by applying the Stokes' theorem

in space and is discretized using the Euler backward scheme in time. The discretized vorticity equation is shown in Equation (4).

$$\begin{aligned} A_i \frac{\omega_i^{n+1} - \omega_i^n}{\Delta t} + \sum_{\partial A} (\boldsymbol{\omega}^{n+1} \times \mathbf{v}^n) \cdot \Delta \mathbf{l} \\ = -\nu \sum_{\partial A} (\nabla \times \boldsymbol{\omega}^{n+1}) \cdot \Delta \mathbf{l} \end{aligned} \quad (4)$$

The convective & stretching term and the diffusive term are further discretized, and the scheme is explained thoroughly by Tian (2014). A hybrid interpolation scheme that couples the first order upwind method, the second order upwind method and the Quadratic Upstream Interpolation for Convective Kinematics (QUICK) method is adopted in this work (Woodfield, 2004).

2.3 Velocity Calculation

The velocity field \mathbf{v} is directly related to the potential vector $\boldsymbol{\psi}$

$$\nabla \times \boldsymbol{\psi} = \mathbf{v} \quad (5)$$

Considering the relationship between velocity and vorticity ($\boldsymbol{\omega} = \nabla \times \mathbf{v}$), we further have

$$\nabla^2 \boldsymbol{\psi} = -\boldsymbol{\omega} \quad (6)$$

Equation (6) is a Poisson's equation, which can be solved through a direct volume integral of the Green's function.

$$\boldsymbol{\psi}(\mathbf{x}_c) = \int_V \frac{\boldsymbol{\omega}(\mathbf{x})}{4\pi|\mathbf{x} - \mathbf{x}_c|} dV + \boldsymbol{\psi}_{in} \quad (7)$$

where \mathbf{x}_c is the point where $\boldsymbol{\psi}$ is calculated, $\boldsymbol{\omega}(\mathbf{x})$ is the vorticity distribution in the computational domain. $\boldsymbol{\psi}_{in}$ is the stream-function vector of the background inflow. The direct integral of Equation (7) is very expensive to conduct in 3-D space. For all the points where velocity is evaluated, the inductions from all the cells with significant vorticity should be considered, which is about N^2 complexity where N is the number of cells.

In order to improve the computational efficiency, an FVM scheme is adopted to solve the Poisson's equation. With proper implementation, the computational complexity can be reduced to be almost proportional to N .

Consider a known velocity field \mathbf{w} which conserves the vorticity in the flow field.

$$\boldsymbol{\omega} = \nabla \times \mathbf{w} \quad (8)$$

However, this vorticity preserving velocity \mathbf{w} does not necessarily satisfy the continuity equation. Therefore, to enforce the divergence-free condition of the velocity field, a potential correction η is introduced to correct the velocity field \mathbf{w} .

$$\mathbf{u} = \mathbf{w} + \nabla \eta \quad (9)$$

By taking the divergence on both sides of Equation (9), the Poisson' equation for η can be obtained

$$\nabla^2 \eta = -\nabla \cdot \mathbf{w} \quad (10)$$

Therefore, the volume integral Equation (7) is only used to calculate the Neumann boundary conditions for the above Poisson's equation.

The calculation of vorticity preserving velocity field \mathbf{w} is not unique. Recall the discretized vorticity equation (4), it is not hard to find that

$$\mathbf{w}^{n+1} = -\Delta t[\boldsymbol{\omega}^{n+1} \times \mathbf{v}^n + \nu \nabla \times \boldsymbol{\omega}^{n+1}] + \mathbf{v}^n \quad (11)$$

2.4 Vorticity Creation

Both the no-slip and non-penetrating boundary conditions of velocity should be satisfied on the wall surface. Since the vorticity field will induce both normal and tangential velocity on the wall in this scheme, a vorticity creation scheme is necessary to enforce the boundary conditions on the wall. The amount of vorticity released from the wall is directly related to the instantaneous flow state.

Assuming we are preparing to march from time step m to time step $m+1$. The vorticity field coming out of Equation (3) at time step m is denoted as $\boldsymbol{\omega}^{m*}$, and the corresponding velocity field determined by Equation (9) is \mathbf{u}^{m*} . The “*” in the superscript indicates the values before vorticity creation, which can be seen as intermediate results of this time step. Now, by adding the inflow velocity \mathbf{U}_{in} , the total velocity at time step m reads

$$\mathbf{v}^{m*} = \mathbf{U}_{in} + \mathbf{u}^{m*} \quad (12)$$

However, the total velocity \mathbf{v}^{m*} is not strictly $\mathbf{0}$ on the wall. There exists normal components \mathbf{v}_n^{m*} and tangential components \mathbf{v}_s^{m*} . A BEM solver is used to enforce the non-penetrating boundary condition by taking the normal velocity \mathbf{v}_n^{m*} as input. The potential distribution ϕ from BEM and the tangential velocity \mathbf{v}_s^{m*} on the wall is then converted to the surface vorticity distribution $\boldsymbol{\gamma}_w$.

$$\boldsymbol{\gamma}_w = -\mathbf{v}_s^{m*} - \nabla_s \phi \quad (13)$$

where $\nabla_s = (\partial/\partial s_1, \partial/\partial s_2)$ is the gradient operator tangential to the wall. The created surface vorticity is released into the domain according to the Stokes’ theorem.

2.6 Pressure Calculation

Since the pressure does not appear in the vorticity equation, it is retrieved by special treatments.

One method of calculating the pressure is through a line integral of the total head H , which is defined in Equation (14).

$$H = \frac{v^2}{2} + \frac{p}{\rho} \quad (14)$$

Also, the gradient of total head reads

$$\nabla H = -\frac{\partial \mathbf{v}}{\partial t} + \mathbf{v} \times \boldsymbol{\omega} - \nu \nabla \times \boldsymbol{\omega} \quad (15)$$

Hence, the total head is calculated by integrating the RHS of Equation (15) along a line in the domain. Further, the pressure can be calculated using Equation (14).

Another way of evaluating the pressure is by making use of the zero velocity on the wall. The momentum equation is simplified as Equation (16) because of the zero velocity on the wall.

$$\nabla \left(\frac{p}{\rho} \right) = -\nu \nabla \times \boldsymbol{\omega} \quad (16)$$

The pressure at a reference point on the wall can be determined by Equation (14) and (15), and the pressure at other locations on the wall can be calculated based on Equation (16).

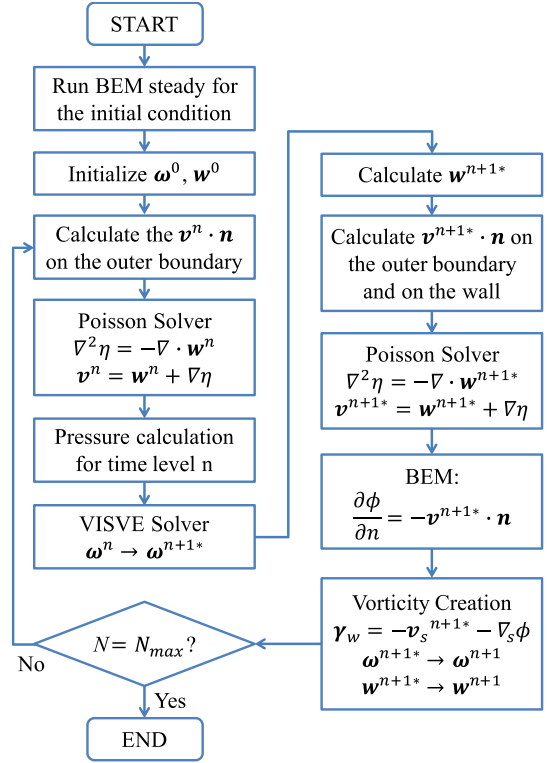


Figure 1 General solving procedures of VISVE

2.5 Rotational Frame

For the flow past a rotating propeller, the flow rotation is considered as a non-inertial frame. Considering the frame is rotating with angular velocity $\boldsymbol{\Omega}$, the total velocity field under the non-inertial frame reads

$$\mathbf{v}_r = \mathbf{v}_i + \boldsymbol{\Omega} \times \mathbf{r} \quad (17)$$

where \mathbf{v}_r is the velocity with respect to the non-inertial frame, and \mathbf{v}_i is the velocity with respect to the inertial frame. \mathbf{r} is the location vector.

Similarly, the vorticity in the non-inertial frame reads

$$\boldsymbol{\omega}_r = \boldsymbol{\omega}_i + 2\boldsymbol{\Omega} \quad (18)$$

where, $\boldsymbol{\omega}_r$ is the vorticity with respect to the non-inertial frame, and $\boldsymbol{\omega}_i$ is the vorticity with respect to the inertial frame.

Considering only the frame rotation, the momentum equation under the non-inertial frame has 3 additional acceleration terms

$$\frac{\partial \mathbf{v}_r}{\partial t} + (\mathbf{v}_r \cdot \nabla) \mathbf{v}_r = -\nabla p + \nu \nabla^2 \mathbf{v}_r - \frac{d\boldsymbol{\Omega}}{dt} \times \mathbf{r} - 2\boldsymbol{\Omega} \times \mathbf{v}_r - \boldsymbol{\Omega} \times (\boldsymbol{\Omega} \times \mathbf{r}) \quad (19)$$

Therefore, the vorticity equation in the non-inertial frame can be obtained by taking curl on Equation (19)

$$\frac{\partial \boldsymbol{\omega}_r}{\partial t} + (\mathbf{v}_r \cdot \nabla) \boldsymbol{\omega}_r = (\boldsymbol{\omega}_r \cdot \nabla) \mathbf{v}_r + \nu \nabla^2 \boldsymbol{\omega}_r - 2 \frac{d\boldsymbol{\Omega}}{dt} + 2(\boldsymbol{\Omega} \cdot \nabla) \mathbf{v}_r \quad (20)$$

By defining

$$\Theta = \omega + 2\Omega \quad (21)$$

and considering the angular velocity Ω to be constant in space, the vorticity equation is simplified as

$$\frac{\partial \Theta}{\partial t} + \nabla \times (\Theta \times v_r) = -\nu \nabla \times (\nabla \times \Theta) \quad (22)$$

Equation (22) demonstrates that the vorticity equation under the non-inertial frame takes the same form as that in the inertial frame.

2.7 General Solving Strategy

The general solving scheme is shown in Figure 1. The flowchart illustrates the connections between all the solvers.

3 NUMERICAL RESULTS

3.1 3-D Hydrofoil of Elliptic Planform

The method is applied to the flow past a 3-D elliptical wing with NACA 66 sections in non-orthogonal grids.

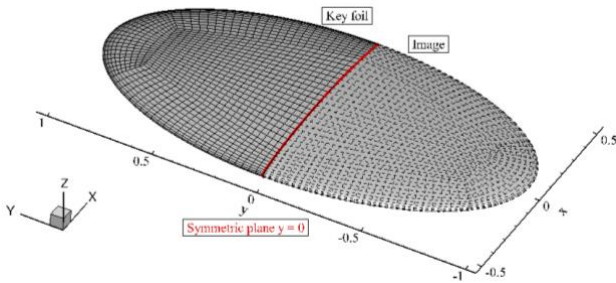


Figure 2 Geometry and surface mesh of the 3-D hydrofoil of elliptic planform

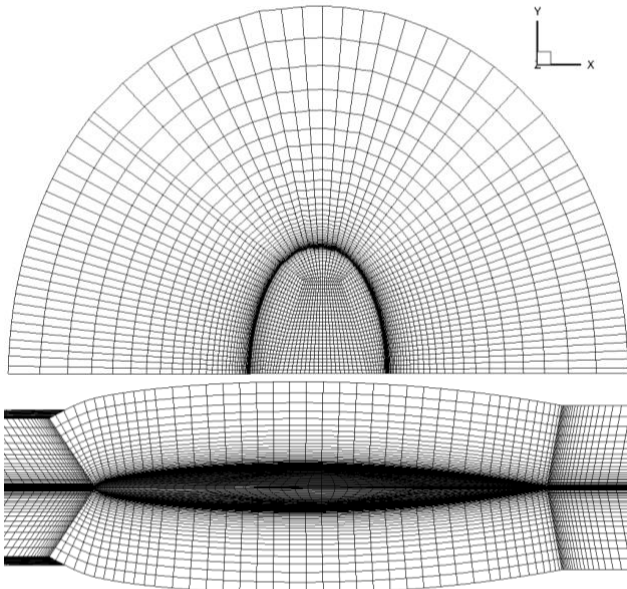


Figure 3 Mesh of the 3-D hydrofoil of elliptic planform

The wing with an aspect ratio of 2 has NACA 66 thickness at all span-wise sections and a closed round tip. The thickness is 10% of the chord length, c , of each section. Half of the width of the wing is set to be equal to the maximum chord length at the span-wise section $y = 0$. The reason for choosing such a wing is to have a 3-D wing

geometry with elliptical plan-form and a blunt leading edge as shown in Figure 2. Also, an image model is adopted in this case as illustrated in Figure 2. The flow domain of image and that of the key foil is symmetric with respect to the plane $y = 0$ and therefore only half of the domain is modeled in VISVE.

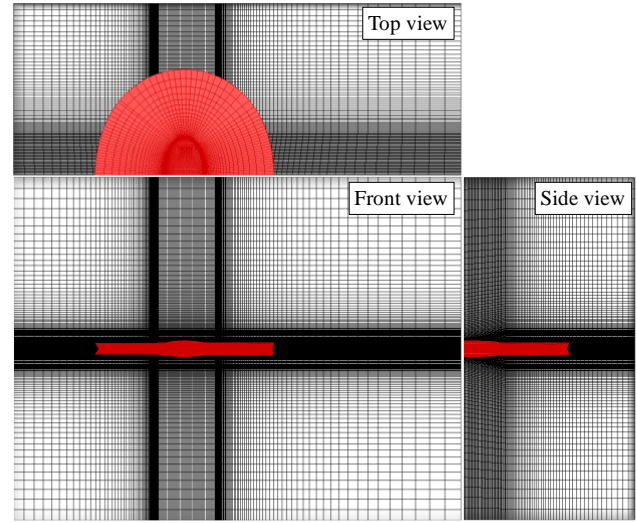


Figure 4 Domain size comparison of the hydrofoil flow between VISVE and N-S (red is VISVE, and black is N-S)

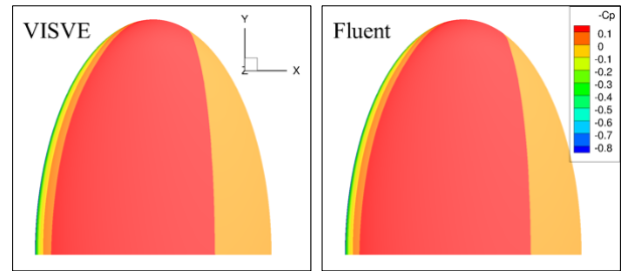


Figure 5 Pressure coefficient distribution on the body surface of 3-D hydrofoil at angle of attack $\alpha = 0^\circ$

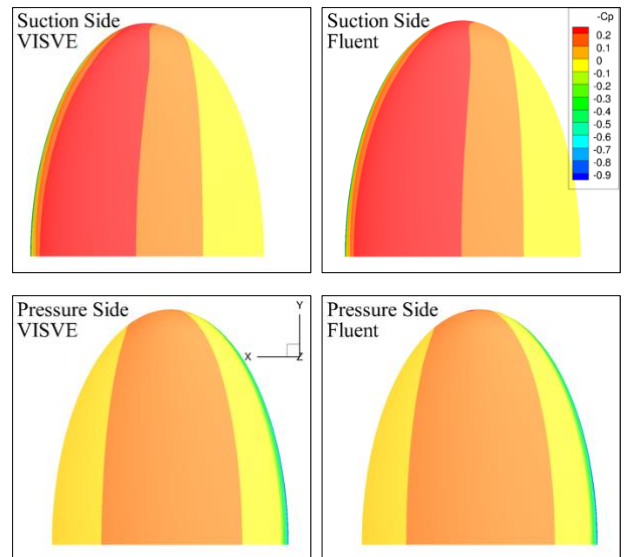


Figure 6 Pressure coefficient distribution on the body surface of 3-D hydrofoil at angle of attack $\alpha = 2^\circ$

The mesh used in VISVE is shown in Figure 3. 181,920 cells are used to discretize the computational domain. In contrast, 4,447,024 hexahedral cells, which is about 30 times of that used in VISVE, are used to discretize the computational domain in N-S simulation. The domain size comparison is shown in Figure 4.

The comparisons of surface pressure coefficient distributions between VISVE and N-S (ANSYS/Fluent, 2018) at Reynolds number $Re = 5000$, defined based on the maximum chord length c as $Re = \frac{Uc}{\nu}$, and angle of attack $\alpha = 0^\circ$ and $\alpha = 2^\circ$ are shown in Figure 5 and Figure 6, respectively. The comparisons of boundary layer profiles between VISVE and an N-S at Reynolds number $Re = 5000$ and angle of attack $\alpha = 0^\circ$ and $\alpha = 2^\circ$ are shown in Figure 12 and Figure 13 in the appendix, in which v_1 , v_2 , and v_3 are the velocity components in x, y, and z direction, respectively.

3.1 NSRCD 4381 Propeller

The VISVE method is also applied to the flow past the NSRCD 4381 propeller, whose geometry is shown in Figure 7. The mesh used in VISVE is shown in Figure 8, and the mesh used in the N-S simulation is shown in Figure 9.

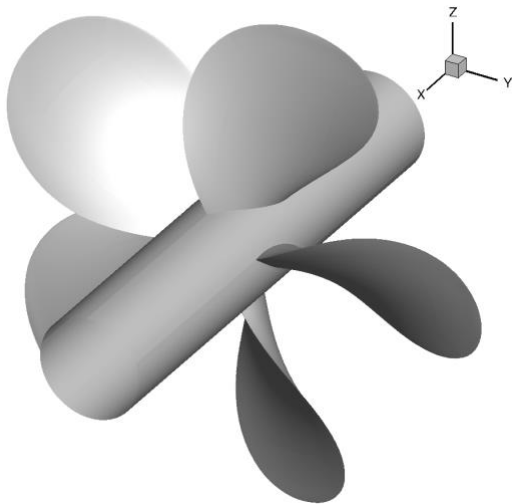


Figure 7 Geometry of the 5 blades NSRCD 4381 propeller

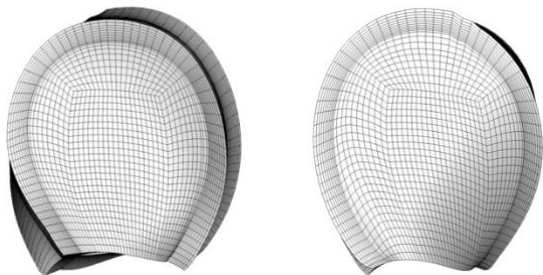


Figure 8 VISVE mesh of the 5 blades NSRCD 4381 propeller

The domain size comparison between VISVE and N-S is shown in Figure 10. In VISVE, 47,500 cells are used to discretize the computational domain. For N-S simulation, 1,476,540 cells are used even with the periodic boundary conditions. The number of cell in VISVE domain is 1/30

of that of N-S domain. Especially in case of a fully unsteady run, the N-S domain is five times larger. In contrast, the domain of VISVE can be kept unchanged since the influence of other blades on the key blade can be taken into consideration in an iterative way.

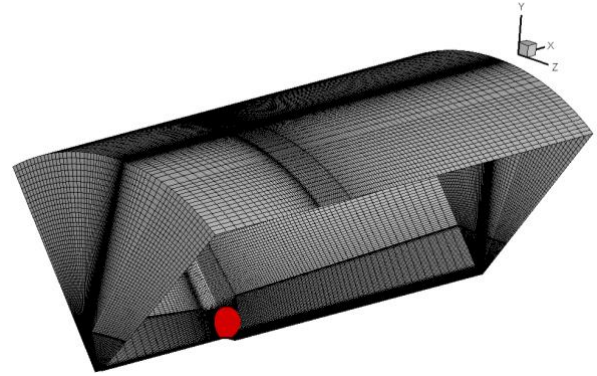


Figure 9 N-S mesh of the 5 blades NSRCD 4381 propeller

Since the grids only cover a small part of the wake, a potential trailing wake model, attached to the end of the grids, is used in VISVE to capture the influence of wake on the propeller (Tian & Kinnas, 2012), as shown in Figure 11. The influence of the wake length covered by the grids is studied as shown in Figure 16 in the appendix, in which the short wake is about 7.8% of the radius and the long wake is about 25.6% of the radius. Note in both cases the potential trailing wake model is utilized after the end of the VISVE wake.

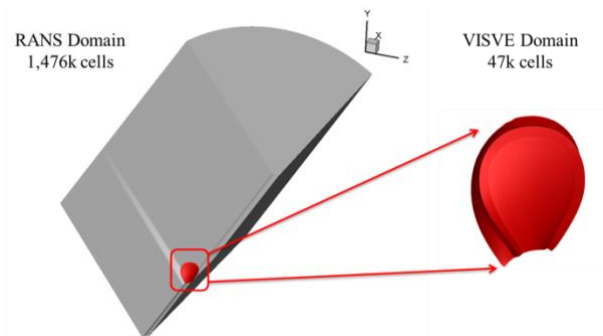


Figure 10 Domain size comparison of the propeller flow between VISVE and N-S (red is VISVE, and black is N-S)

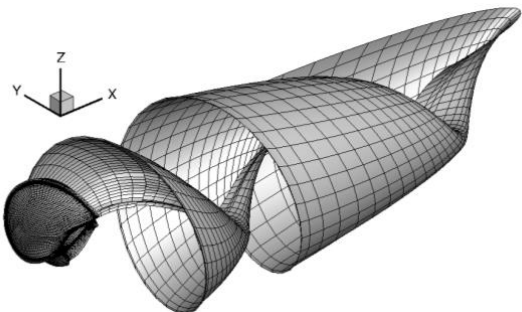


Figure 11 Potential wake attached to the VISVE domain

Comparisons of boundary layer profiles between VISVE and N-S at Reynolds number $Re = 5000$, defined in terms of the diameter of propeller D as $Re = \frac{UD}{\nu}$, and advance ratio $J = 0.889$ and $J = 1.2$ are shown in Figure 14 and Figure 15 in the appendix. In addition, a grid dependence

study is conducted. The grids with different cell number combinations are given in Table 1 and Table 2. The results are shown in Figure 17 and 18 in the appendix. Also, in these figures, v_1 , v_2 , and v_3 are the velocity components in x, y, and z direction, respectively.

Table 1 Grid dependence study in the normal direction

	First Layer Height/R	Expansion Ratio	Number of Layers
Grid 0	0.001	1.2	15
Grid 1	0.0015	1.2	13
Grid 2	0.002	1.2	12
Grid 3	0.001	1.15	18
Grid 4	0.001	1.25	14

Table 2 Grid dependence study in the span-wise and chord-wise directions

	Number in Span-wise direction	Number in Span-wise direction
Grid 0	31	72
Grid 5	36	82
Grid 6	41	92

3 CONCLUSIONS AND FUTURE WORK

A 3-D VIScous Vorticity Equation (VISVE) method is presented to solve the viscous incompressible flow past a 3-D hydrofoil and a propeller. The method is designed to be compact in space and efficient in time.

The proposed method is applied to a 3-D elliptical planform hydrofoil with NACA 66 sections. The thickness is 10% of the chord length at each span-wise section. The inflow comes at an angle of attack $\alpha = 0^\circ$ and $\alpha = 2^\circ$ with Reynolds number $Re = 5000$. The velocity field from VISVE agrees well with that from N-S. The results show that this method is reliable in predicting the flow past a hydrofoil.

In addition, some preliminary results of the flow past a rotating propeller are also presented in this work. A 5 blades NSRCD-4381 propeller at advance ratio $J = 0.889$ and $J = 1.2$ is considered here. The results do not correlate as well with those of N-S, despite the fact that the boundary layer behavior is similar in all directions. The discrepancy between the VISVE and N-S results might be due to the improper implementation of the rotation frame. Further validations are necessary.

The turbulence model is currently implemented into the 2-D VISVE by considering the turbulent viscosity in the vorticity equation. The eddy viscosity is determined by coupling with the OpenFOAM code. Results for the turbulent flow past a 2-D hydrofoil and a 2-D cylinder will be presented in the 29th International Symposium on Ocean and Polar Engineering (ISOPE) conference (Hao & Kinnas, 2019).

The ultimate goal is to develop an efficient numerical tool to model the tip vortex flow and tip gap flow past a propeller to accurately predict the cavitation inception.

Also, this method should be easily switched between forward condition and backing condition.

4 ACKNOWLEDGEMENTS

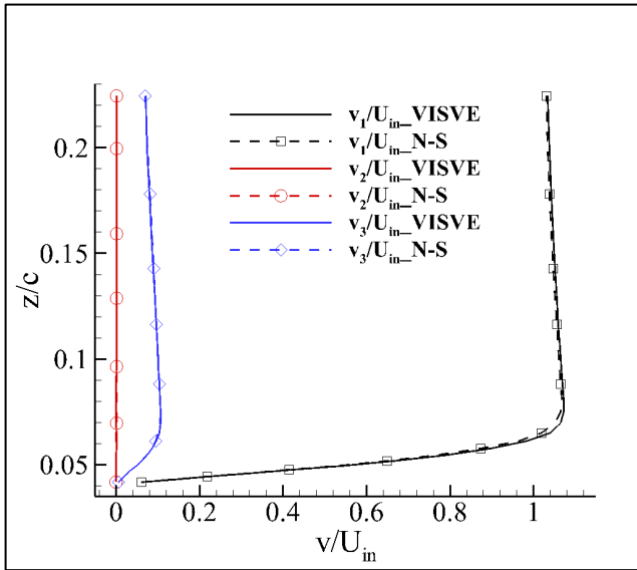
Support for this research was provided by the U.S. Office of Naval Research (Grant Nos. N00014-14-1-0303 and N00014-18-1-2276; Dr. Ki-Han Kim) partly by Phases VII and VIII of the ‘‘Consortium on Cavitation Performance of High Speed Propulsors’’. The authors are grateful for the inspiring ideas provided by Dr. Ye Tian to complete this method, as well as the support. The authors also acknowledge the Texas Advanced Computing Center (TACC) at The University of Texas at Austin for providing HPC resources that have contributed to the research results reported within this paper.

REFERENCES

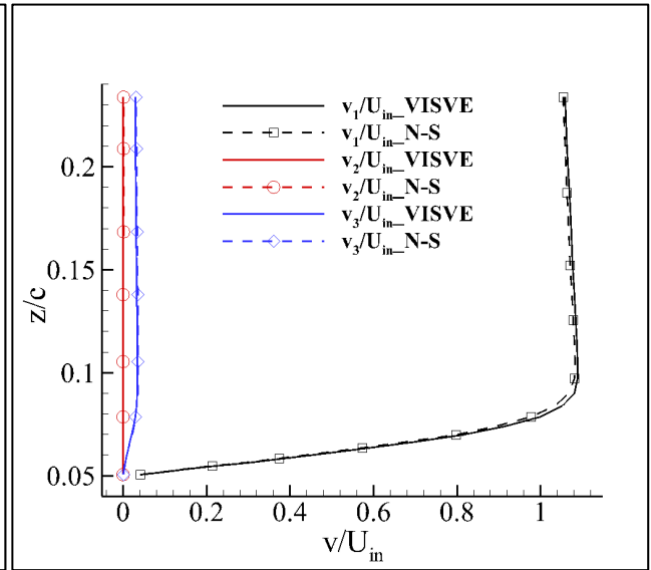
- Almgren, A. S., Buttko, T., and Colella, P. (1994). A fast adaptive vortex method in three dimensions. *Journal of computational Physics*, 113(2):177–200.
- Chorin, A. J. (1981). Estimates of intermittency, spectra, and blow-up in developed turbulence. *Communications on Pure and Applied Mathematics*, 34(6):853–866.
- Degond, P. and Mas-Gallic, S. (1989). The weighted particle method for convection-diffusion equations. i. the case of an isotropic viscosity. *Mathematics of computation*, 53(188):485–507.
- Fluent, A. N. S. Y. S. (2018). ‘‘Ansys fluent.’’ *Academic Research. Release*.
- Leonard, A. (1980). Vortex methods for flow simulation. *Journal of Computational Physics*, 37(3):289–335.
- Leonard, A. (1985). Computing three-dimensional incompressible flows with vortex elements. *Annual Review of Fluid Mechanics*, 17(1):523–559.
- Li, Z. and Kinnas, S.A. (2017). VISVE, a Vorticity Based Model Applied to Unidirectional and Alternating Flow around a Cylinder, *22nd SNAME Offshore Symposium*, Houston, Texas, USA.
- Rehbach, C. (1978). Numerical calculation of three-dimensional unsteady flows with vortex sheets. *16th Aerospace Sciences Meeting*, page 111.
- Saffman, P. (1981). Vortex interactions and coherent structures in turbulence. *Transition and turbulence*, pages 149–166. Elsevier.
- Tian, Y. and Kinnas, S.A. (2012). A wake model for the prediction of propeller performance at low advance ratios. *International Journal of Rotating Machinery*.
- Tian, Y. (2014). Leading Edge and Tip Gap Vortex Tracking and its Effect on Propulsor Performance, *PH.D. dissertation*, UT Austin.
- Tian, Y., Kinnas, S.A. (2015). A Viscous Vorticity Method for Propeller Tip Flows and Leading Edge Vortex, *Fourth International Symposium on Marine Propulsors*, Austin, Texas, USA.
- Tryggvason, G., Dahm, W., and Sbeih, K. (1991). Fine structure of vortex sheet rollup by viscous and inviscid

- simulation. Journal of Fluids Engineering, 113(1):31–36.
- Wu, C., Xing, L. and Kinnas, S.A. (2018). A VIScous Vorticity Equation (VISVE) method applied to 2-D and 3-D hydrofoil in both forward and backing conditions, 23rd SNAME Offshore Symposium, Houston, Texas, USA.
- Wu, C. and Kinnas, S.A. (2019). A Distributed Vorticity Model for Flow Past a 3-D Hydrofoil, 24th SNAME Offshore Symposium, Houston, Texas, USA.
- Xing, L., Wu, C., and Kinnas, S.A. (2018). VISVE, a Vorticity Based Model Applied to Cavitating Flow around a 2-D Hydrofoil, 10th International Symposium on Cavitation, Baltimore, Maryland, USA.
- Yao, H. and Kinnas, S.A. (2019). Coupling Viscous Vorticity Equation (VISVE) Method with OpenFOAM to Predict Turbulent Flow around 2-D Hydrofoils and Cylinders, 29th International Symposium on Ocean and Polar Engineering (ISOPE) conference, Honolulu, Hawaii, USA, June 16-21 (to be presented)

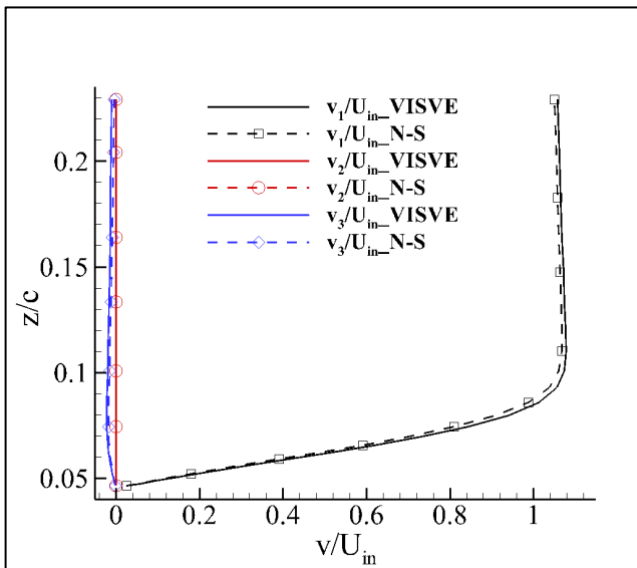
APPENDIX



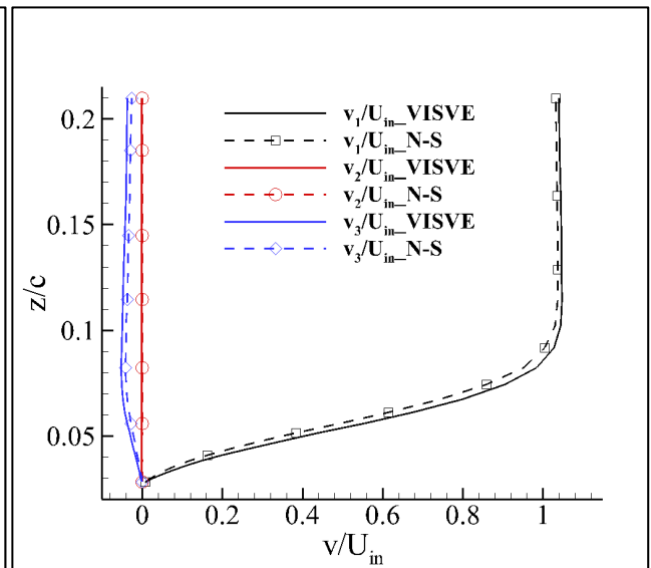
$x/c = 21\%$, $y/c = 7\%$



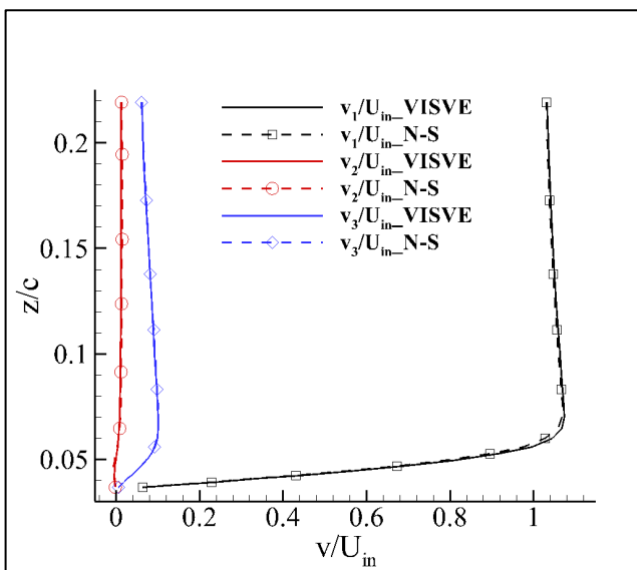
$x/c = 42\%$, $y/c = 7\%$



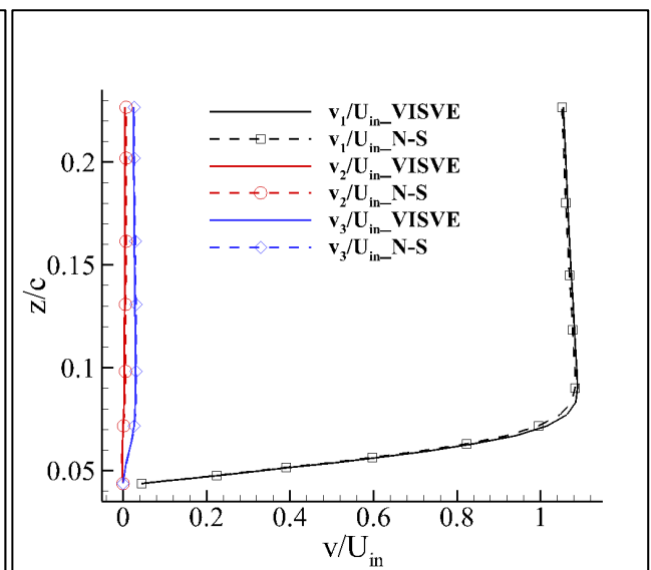
$x/c = 62\%$, $y/c = 7\%$



$x/c = 82\%$, $y/c = 7\%$



$x/c = 21\%$, $y/c = 52\%$



$x/c = 43\%$, $y/c = 52\%$

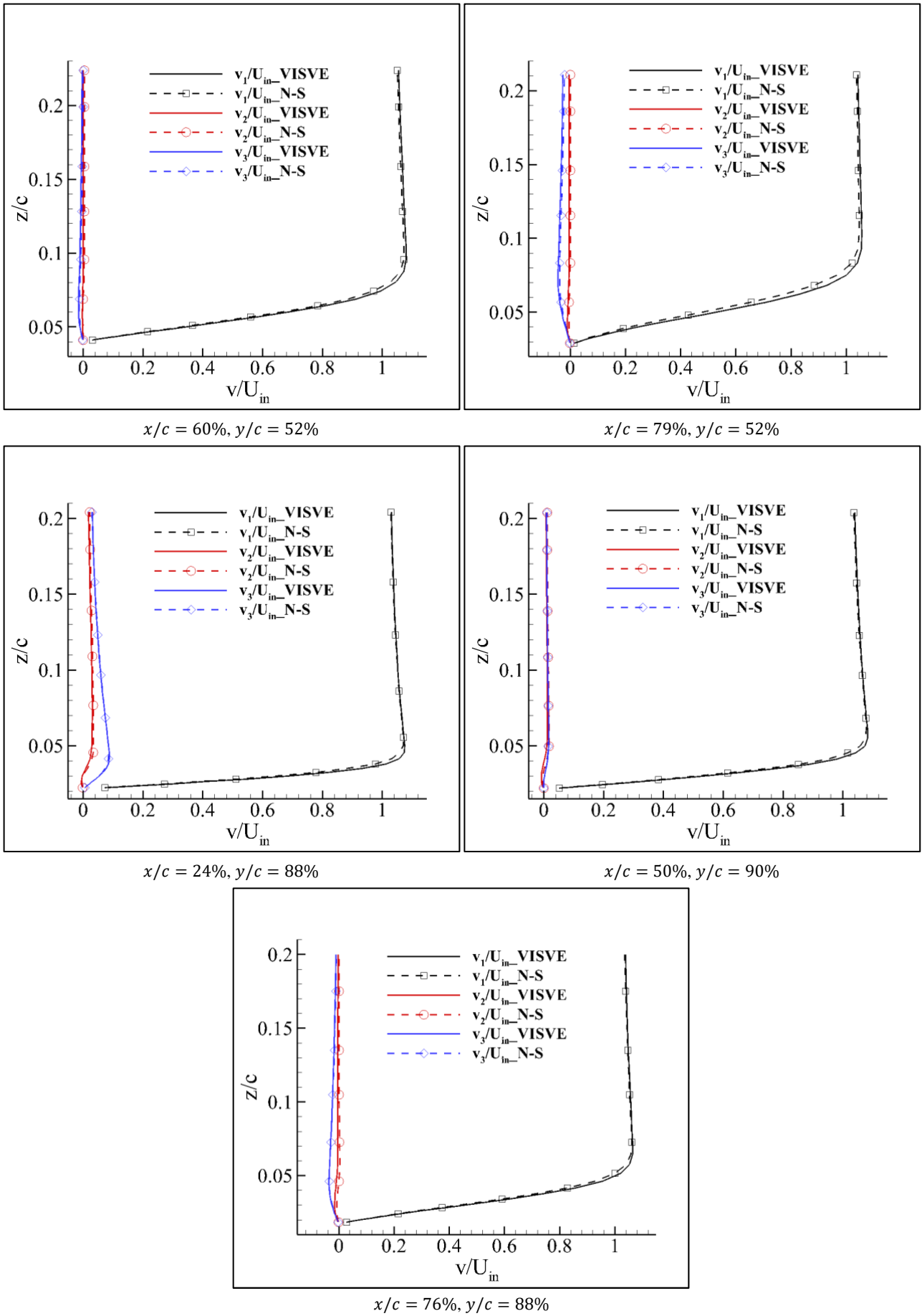
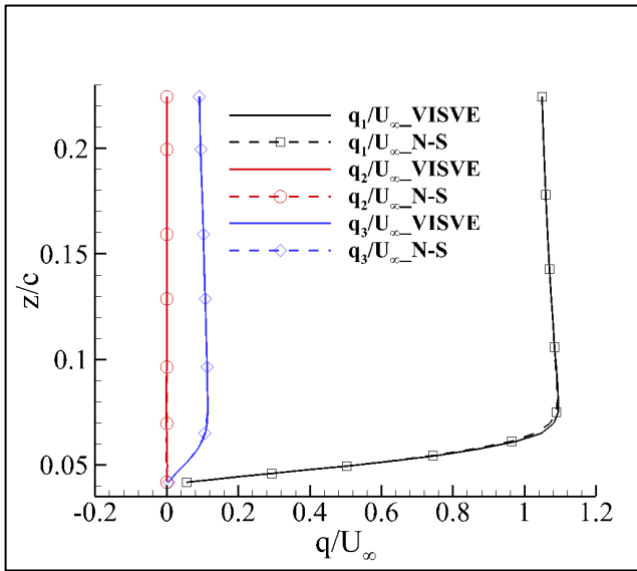
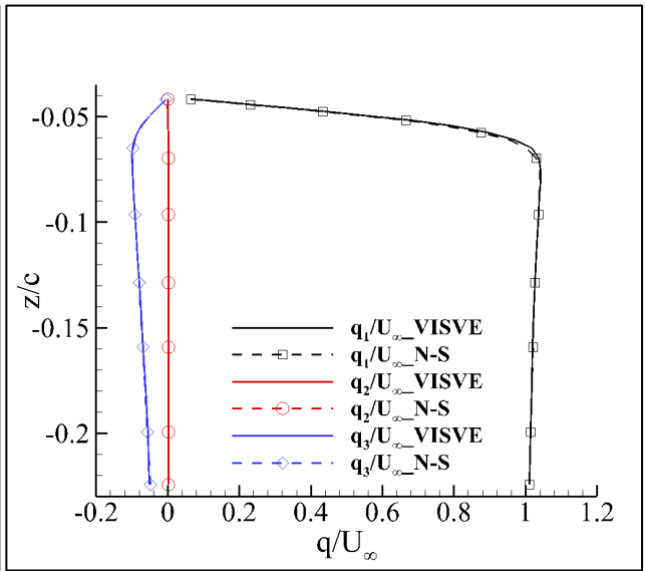


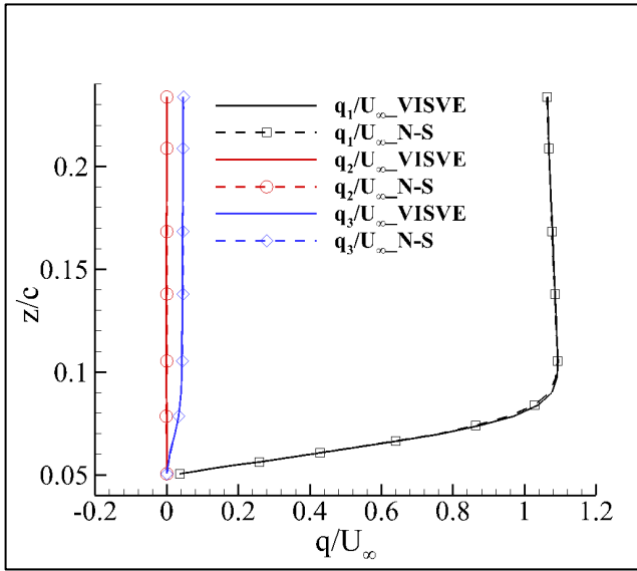
Figure 12 Boundary layer profiles of the elliptical wing at Reynolds number $Re = 5000$ and angle of attach $\alpha = 0^\circ$



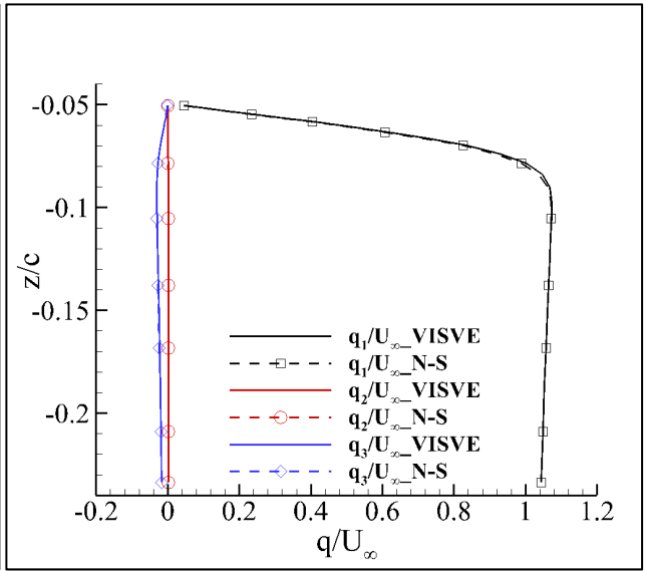
$x/c = 21\%$, $y/c = 7\%$, suction side



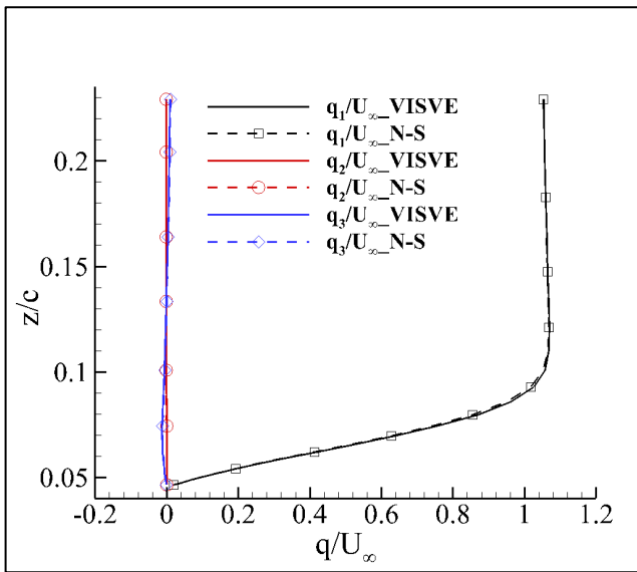
$x/c = 21\%$, $y/c = 7\%$, pressure side



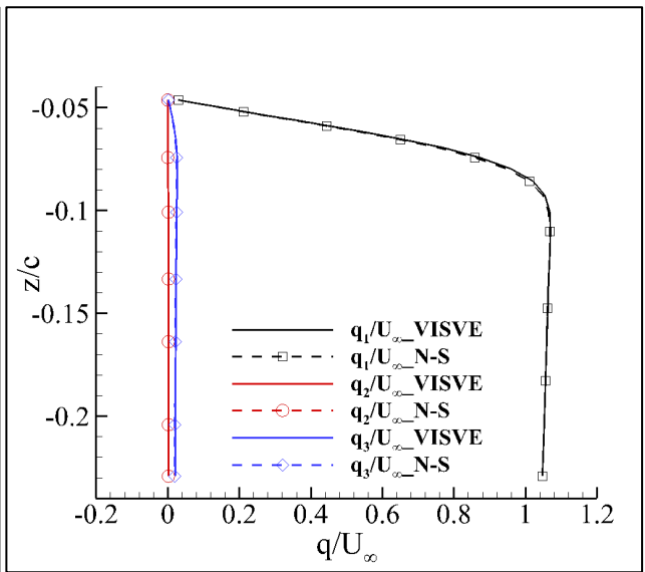
$x/c = 42\%$, $y/c = 7\%$, suction side



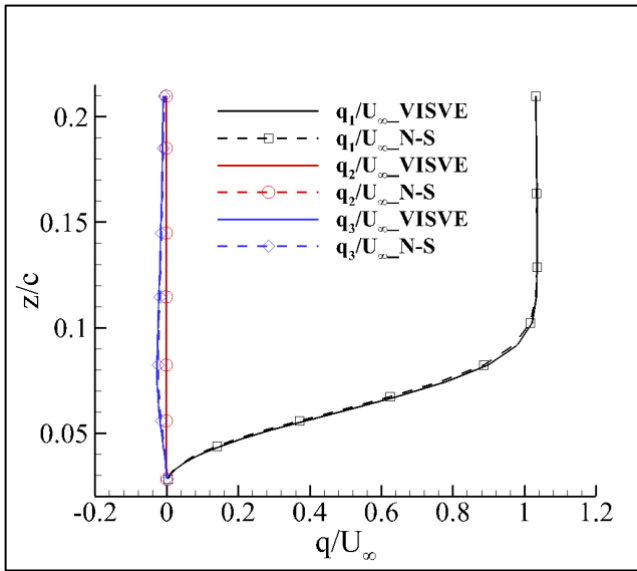
$x/c = 42\%$, $y/c = 7\%$, pressure side



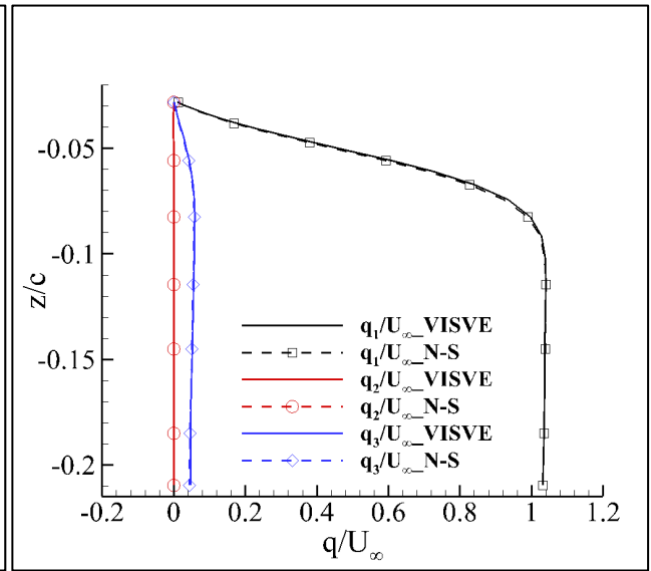
$x/c = 62\%$, $y/c = 7\%$, suction side



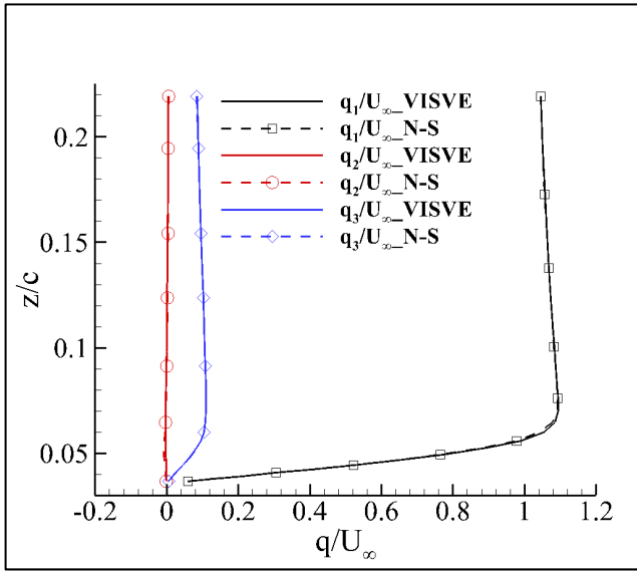
$x/c = 62\%$, $y/c = 7\%$, pressure side



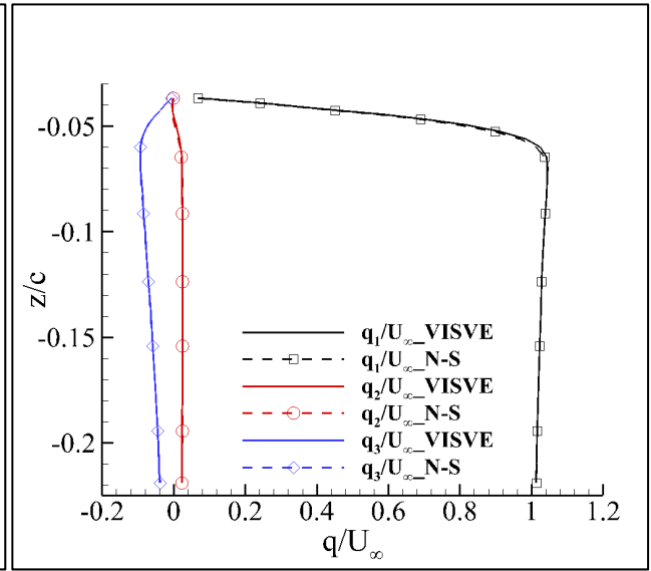
$x/c = 82\%$, $y/c = 7\%$, suction side



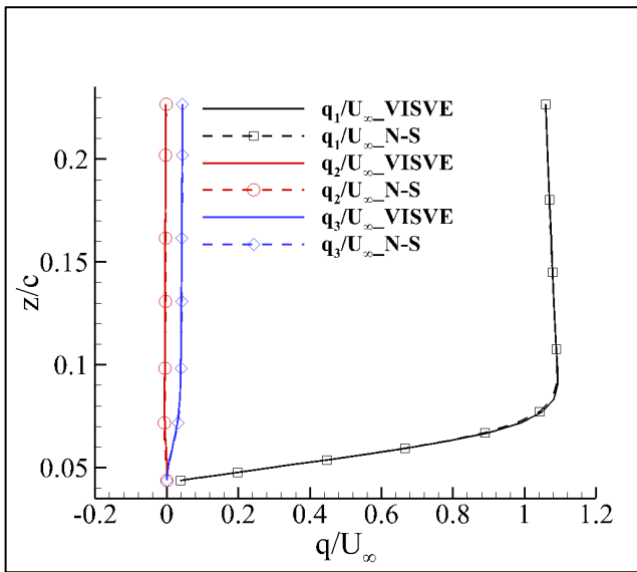
$x/c = 82\%$, $y/c = 7\%$, pressure side



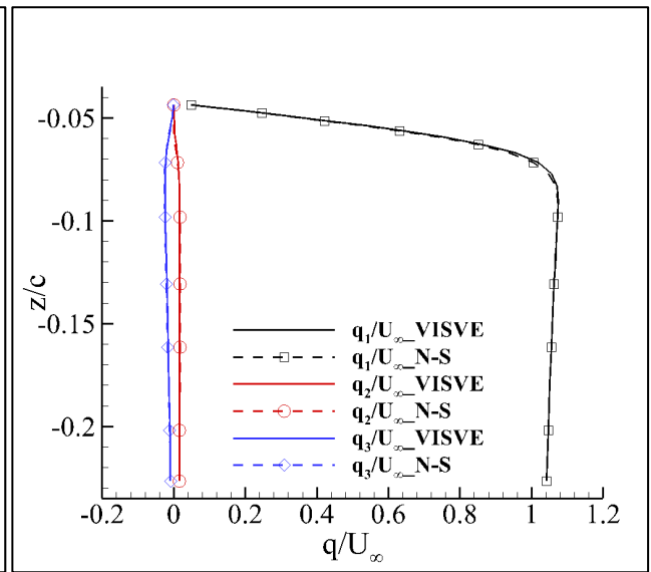
$x/c = 21\%$, $y/c = 52\%$, suction side



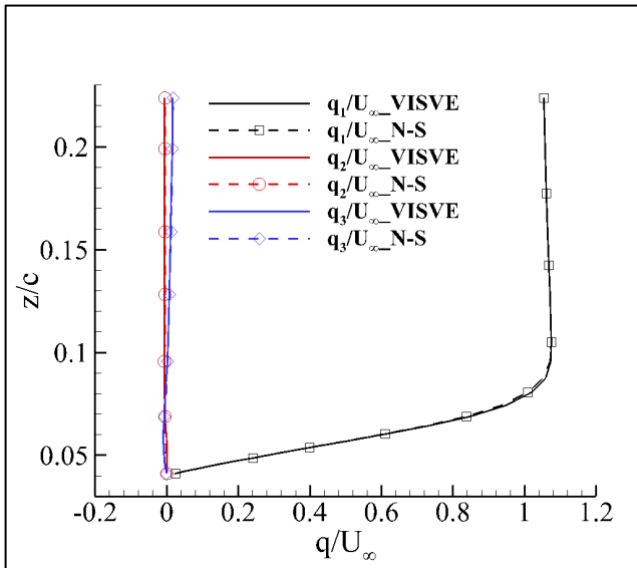
$x/c = 21\%$, $y/c = 52\%$, pressure side



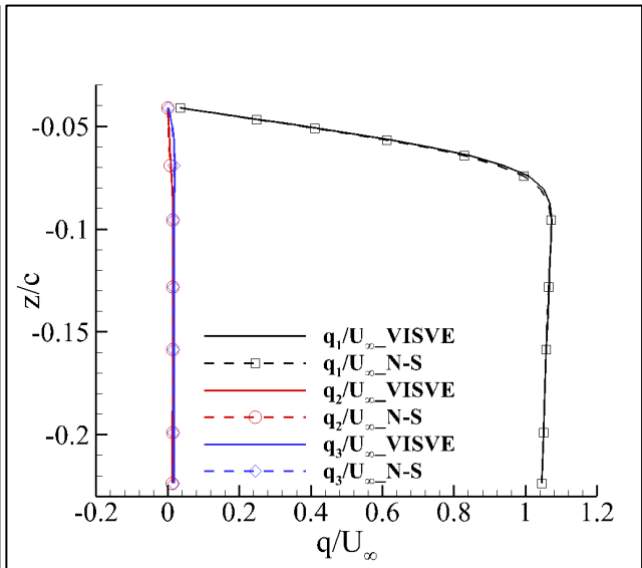
$x/c = 43\%$, $y/c = 52\%$, suction side



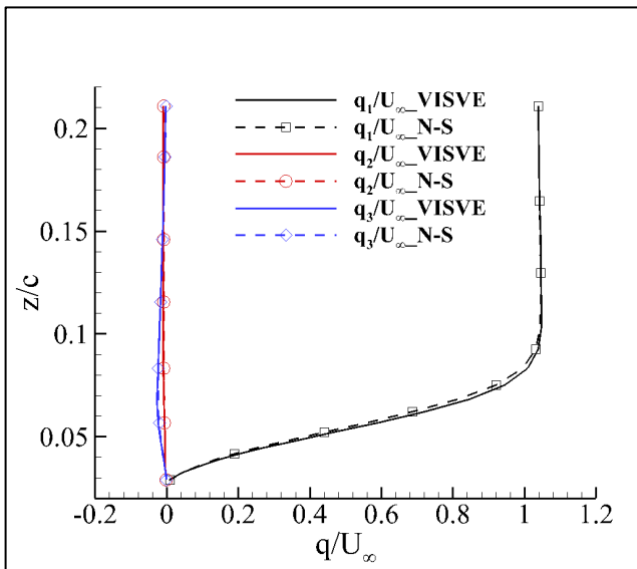
$x/c = 43\%$, $y/c = 52\%$, pressure side



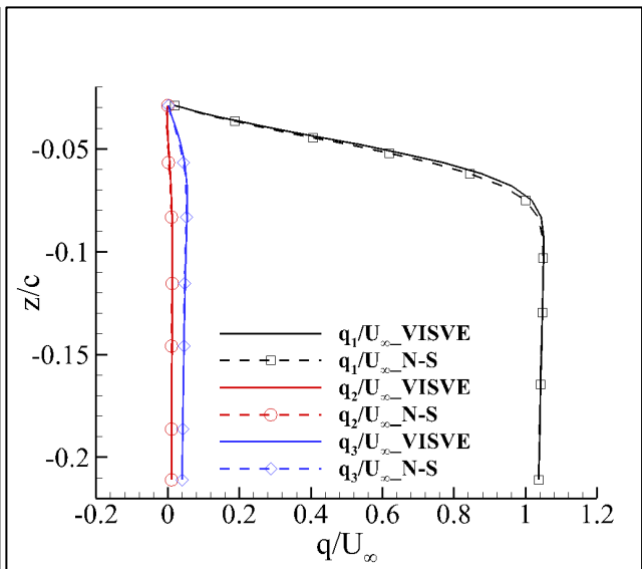
$x/c = 60\%$, $y/c = 52\%$, suction side



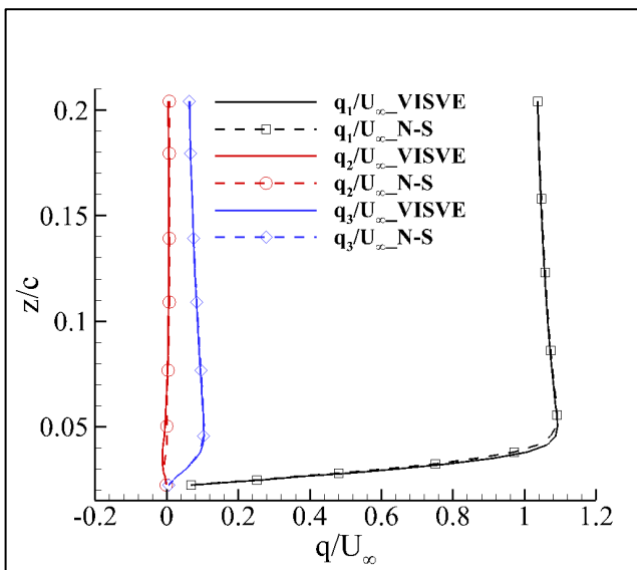
$x/c = 60\%$, $y/c = 52\%$, pressure side



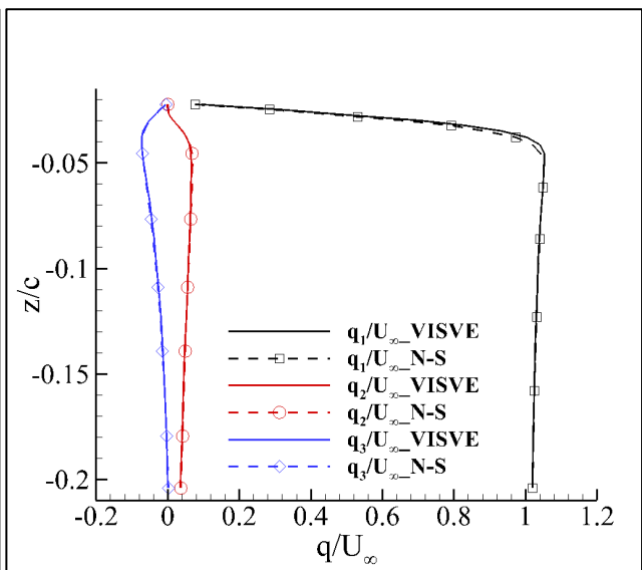
$x/c = 79\%$, $y/c = 52\%$, suction side



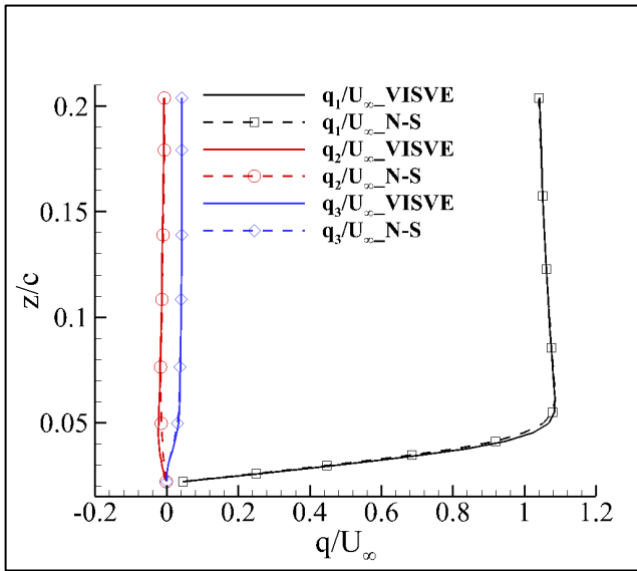
$x/c = 79\%$, $y/c = 52\%$, pressure side



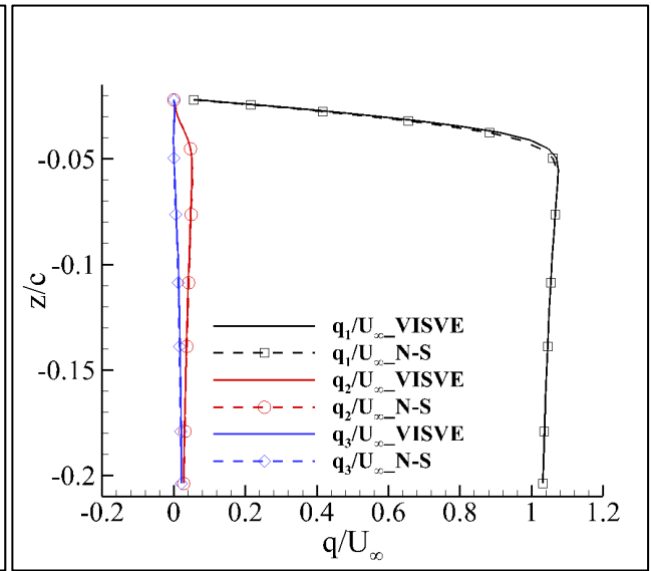
$x/c = 24\%$, $y/c = 88\%$, suction side



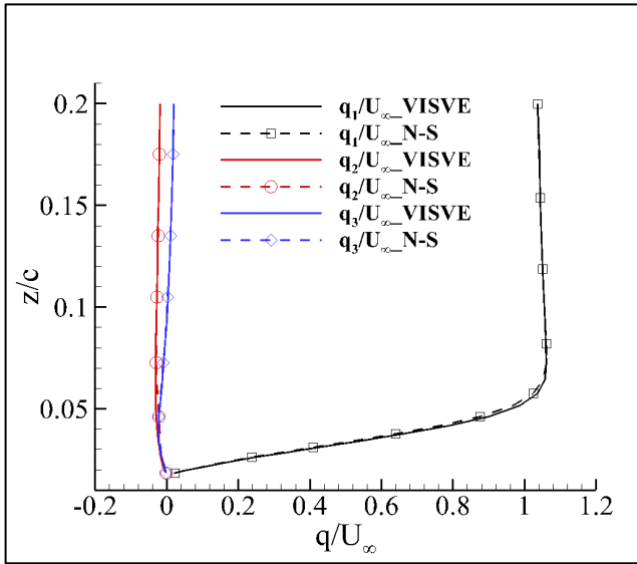
$x/c = 24\%$, $y/c = 88\%$, pressure side



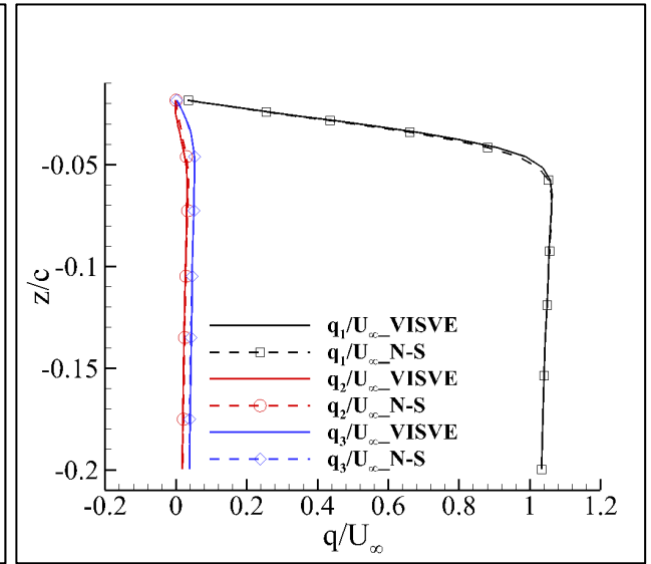
$x/c = 50\%$, $y/c = 90\%$, suction side



$x/c = 50\%$, $y/c = 90\%$, pressure side

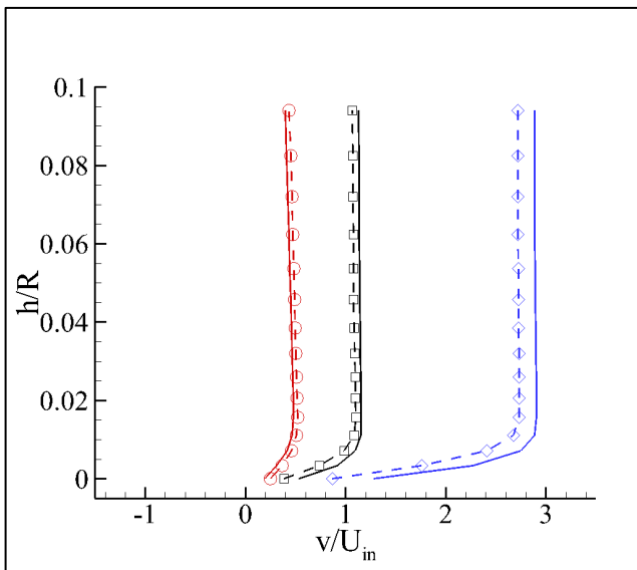


$x/c = 76\%$, $y/c = 88\%$, suction side

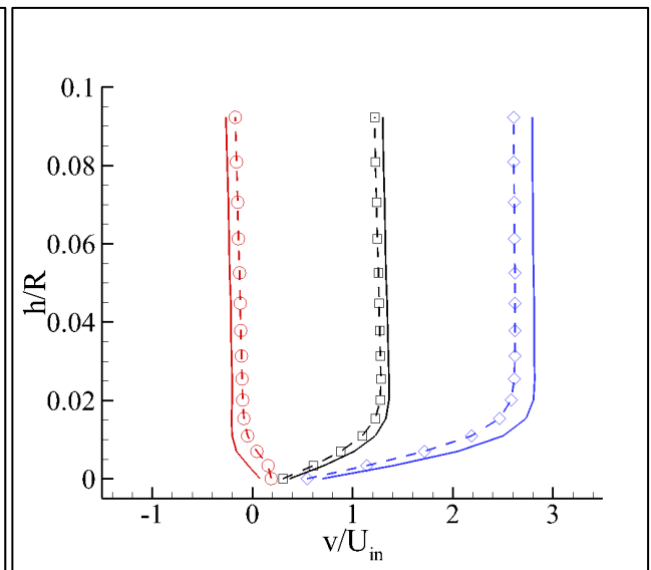


$x/c = 76\%$, $y/c = 88\%$, pressure side

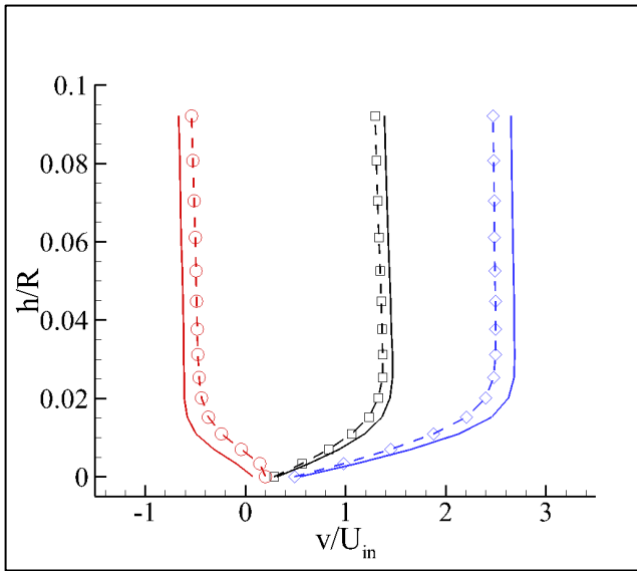
Figure 13 Boundary layer profiles of the elliptical wing at Reynolds number $Re = 5000$ and angle of attach $\alpha = 2^\circ$



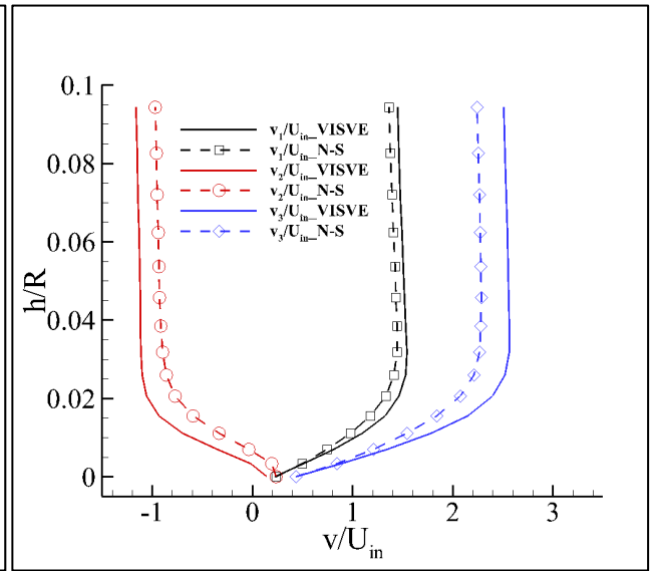
$x/c = 18\%$, $y/R = 73\%$, suction side



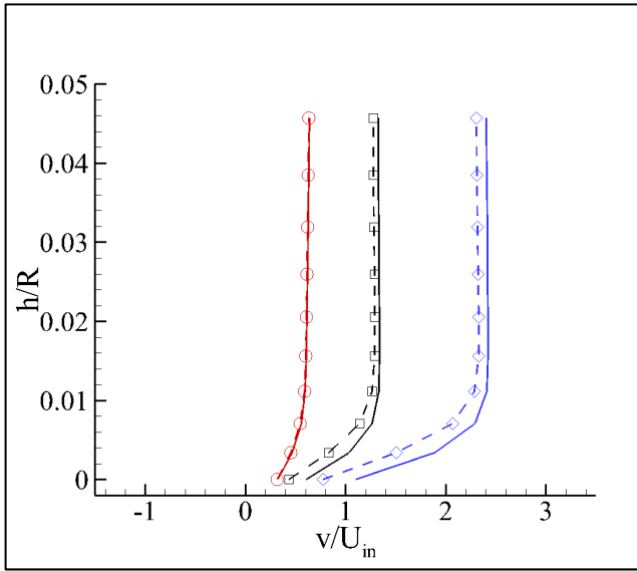
$x/c = 43\%$, $y/R = 71\%$, suction side



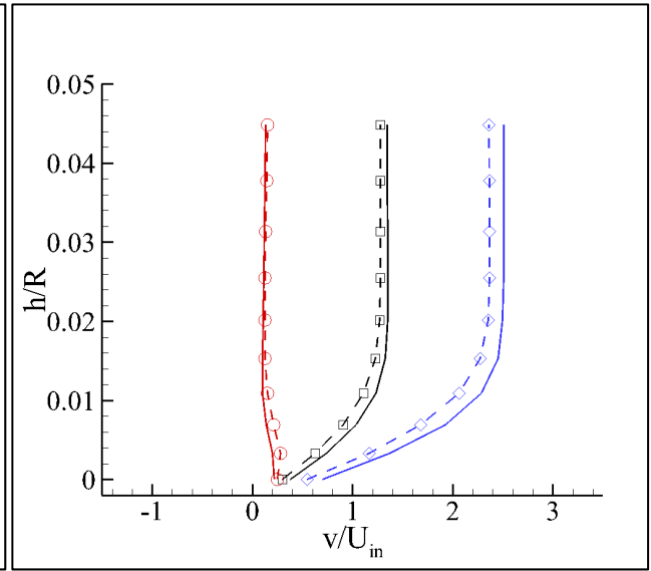
$x/c = 60\%$, $y/R = 71\%$, suction side



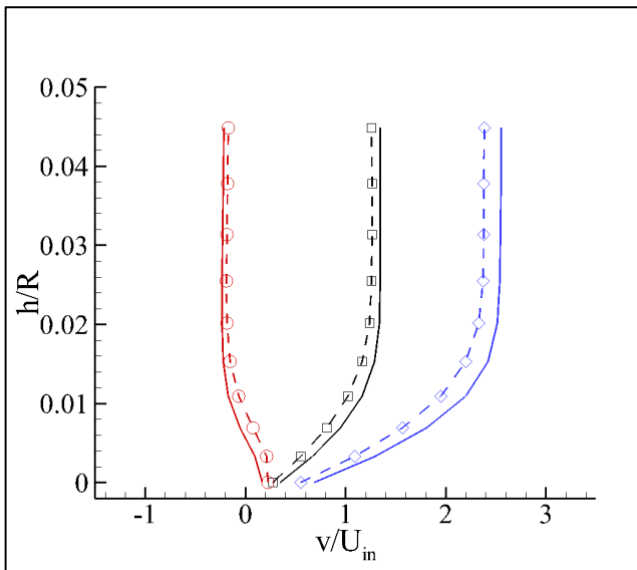
$x/c = 82\%$, $y/R = 73\%$, suction side



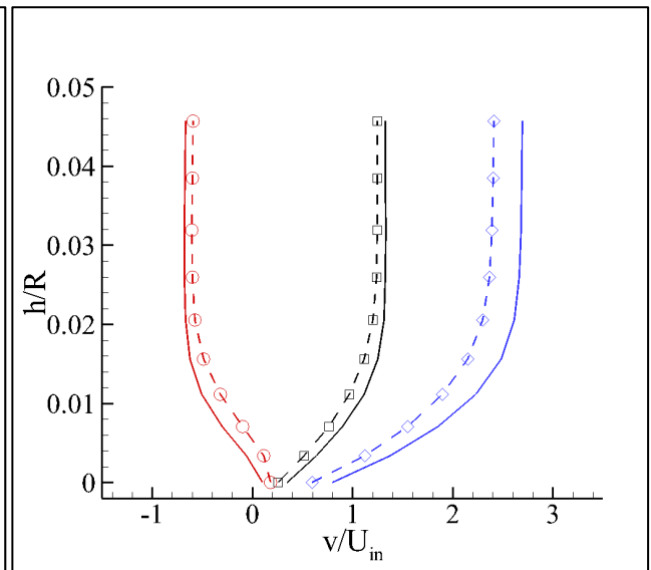
$x/c = 18\%$, $y/R = 73\%$, pressure side



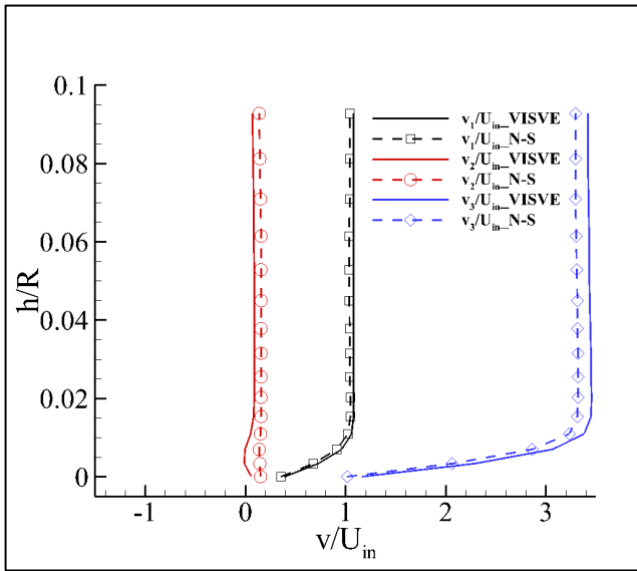
$x/c = 43\%$, $y/R = 71\%$, pressure side



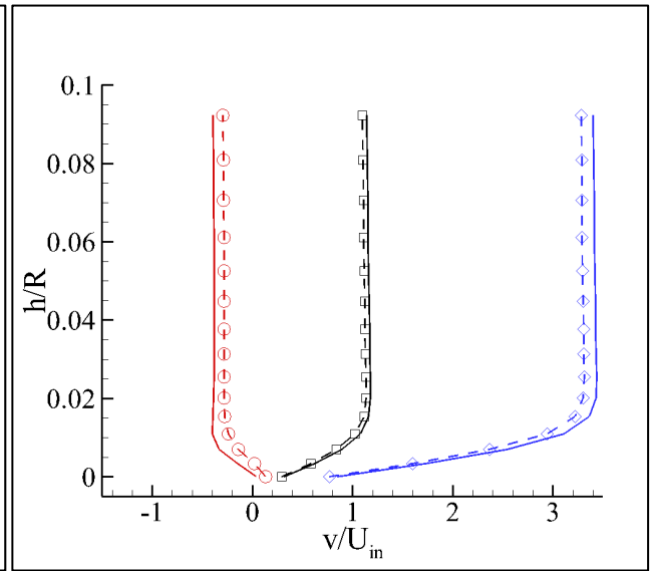
$x/c = 60\%$, $y/R = 71\%$, pressure side



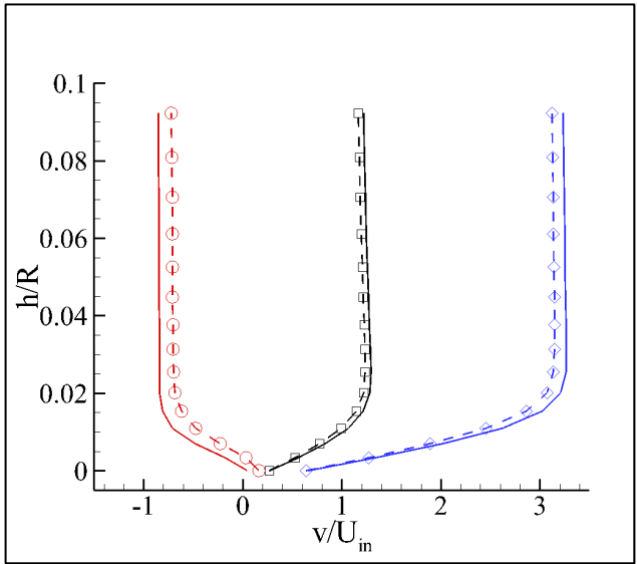
$x/c = 82\%$, $y/R = 73\%$, pressure side



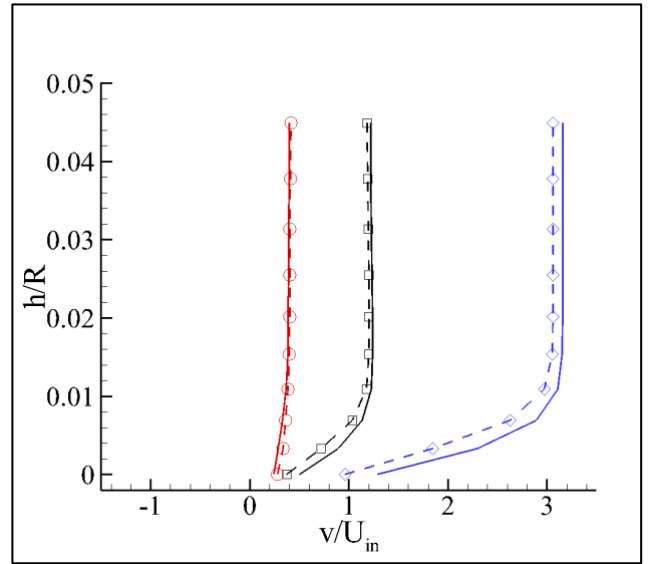
$x/c = 25\%$, $y/R = 90\%$, suction side



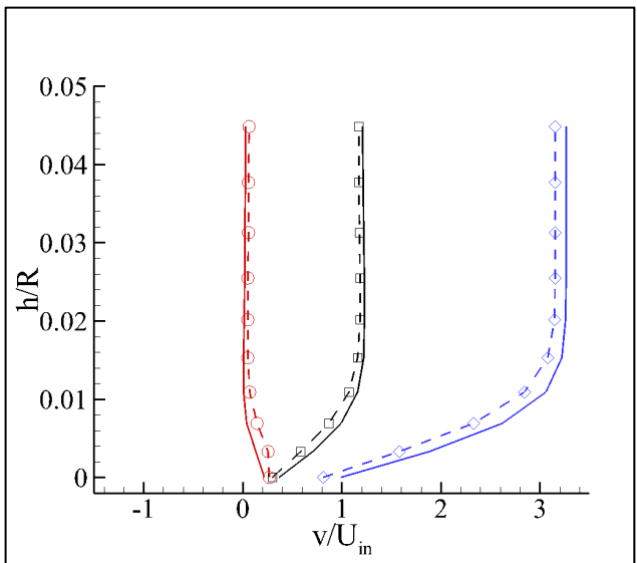
$x/c = 50\%$, $y/R = 90\%$, suction side



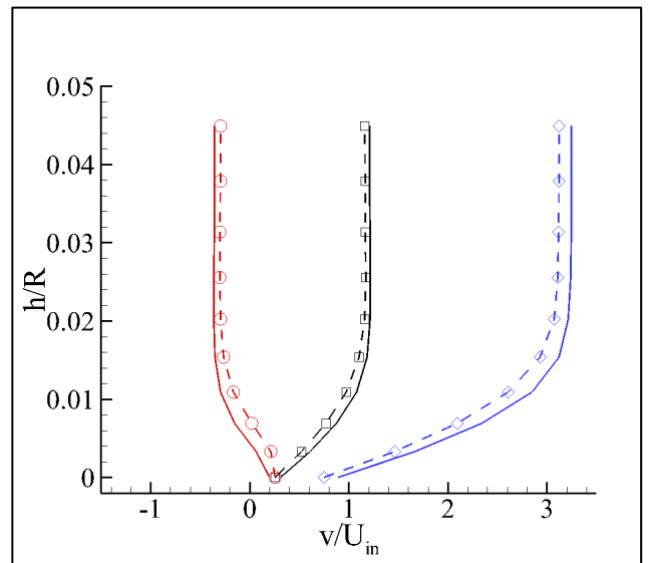
$x/c = 75\%$, $y/R = 90\%$, suction side



$x/c = 25\%$, $y/R = 90\%$, pressure side

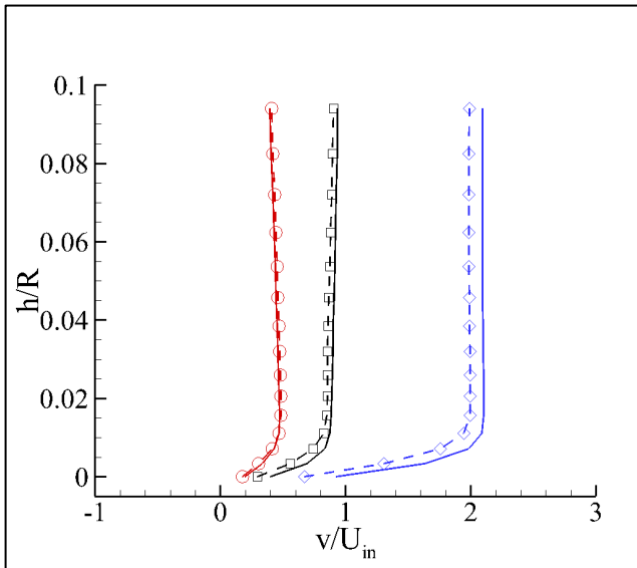


$x/c = 50\%$, $y/R = 90\%$, pressure side

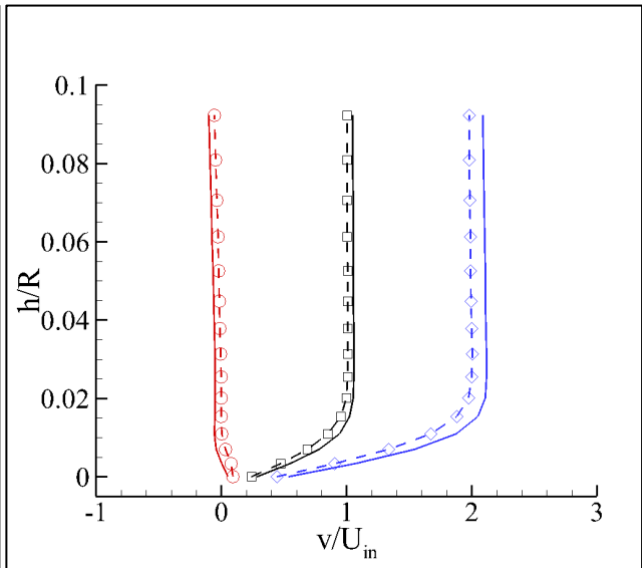


$x/c = 75\%$, $y/R = 90\%$, pressure side

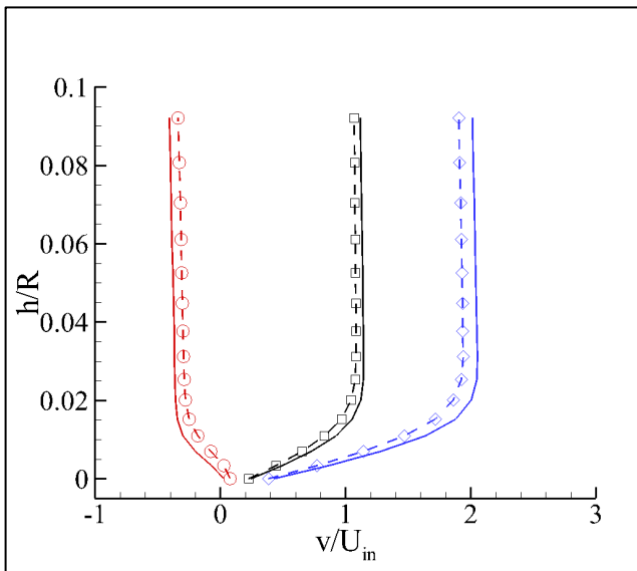
Figure 14 Boundary layer profiles of the propeller at Reynolds number $Re = 5000$ and advance ratio $J = 0.889$



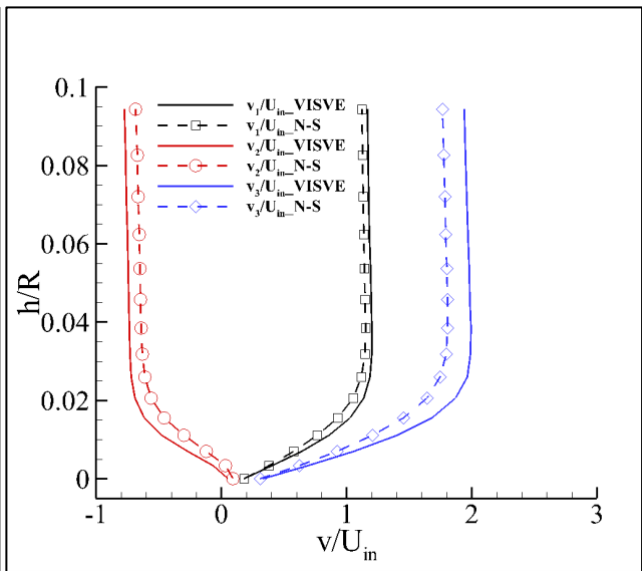
$x/c = 18\%$, $y/R = 73\%$, suction side



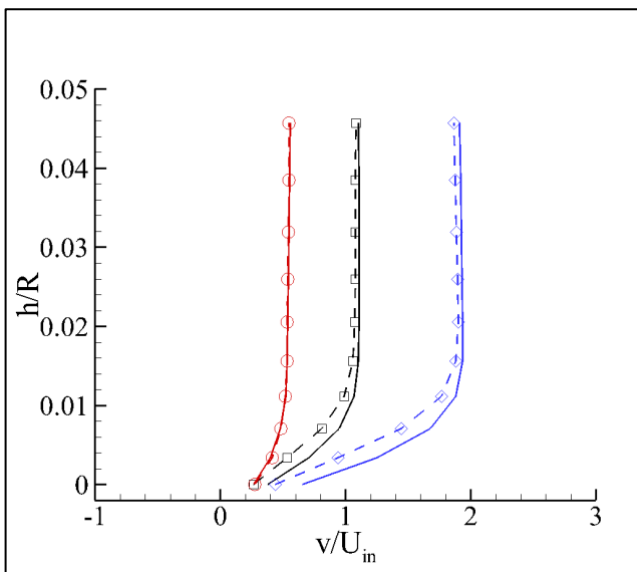
$x/c = 43\%$, $y/R = 71\%$, suction side



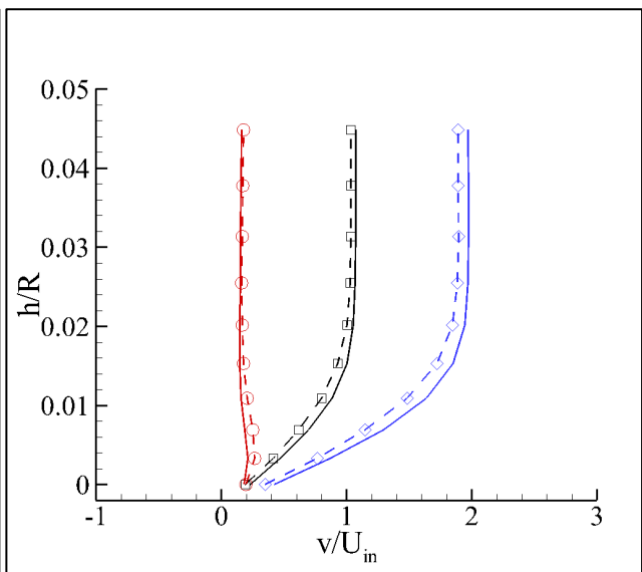
$x/c = 60\%$, $y/R = 71\%$, suction side



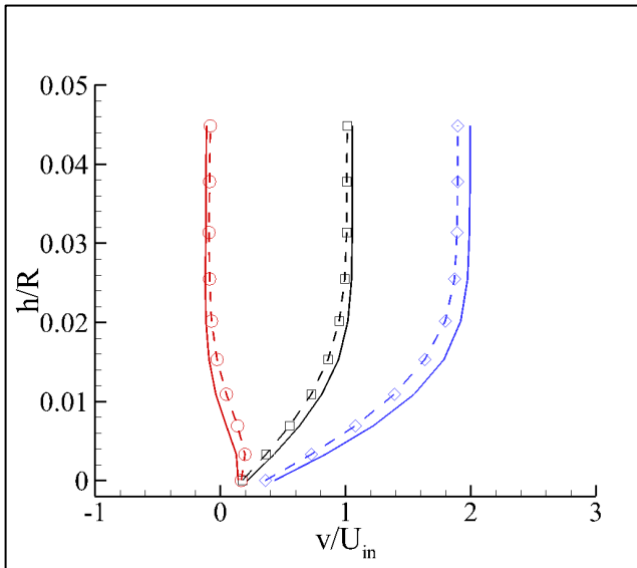
$x/c = 82\%$, $y/R = 73\%$, suction side



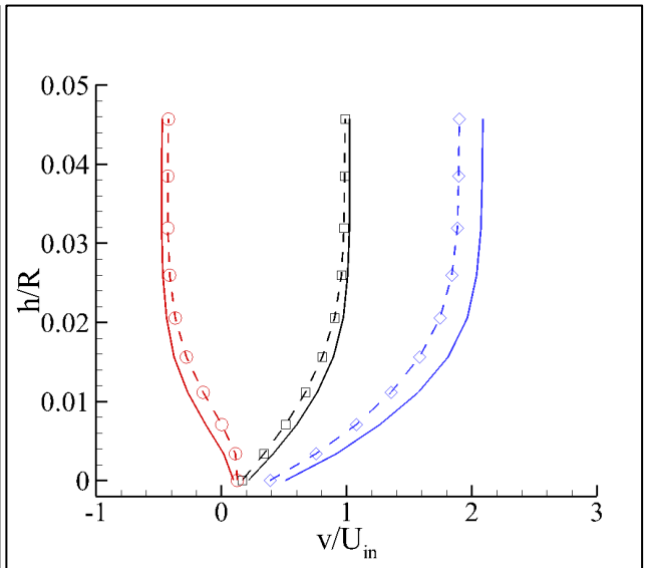
$x/c = 18\%$, $y/R = 73\%$, pressure side



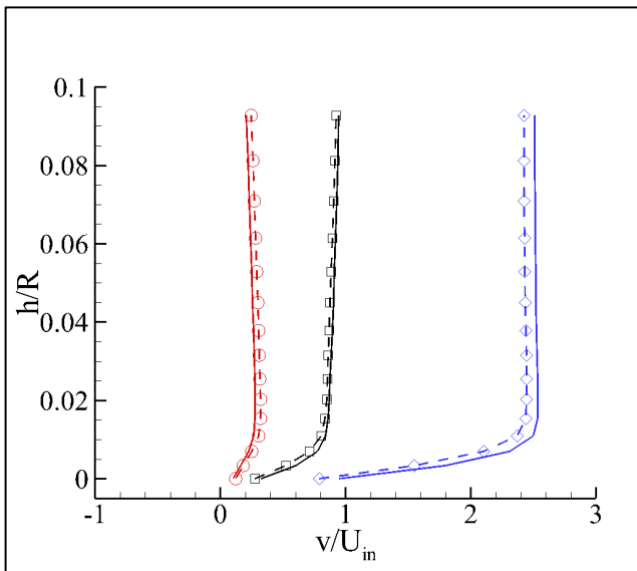
$x/c = 43\%$, $y/R = 71\%$, pressure side



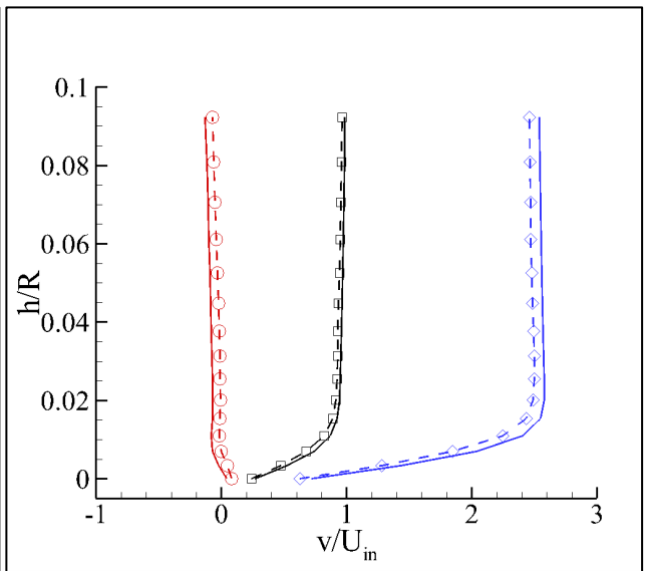
$x/c = 60\%$, $y/R = 71\%$, pressure side



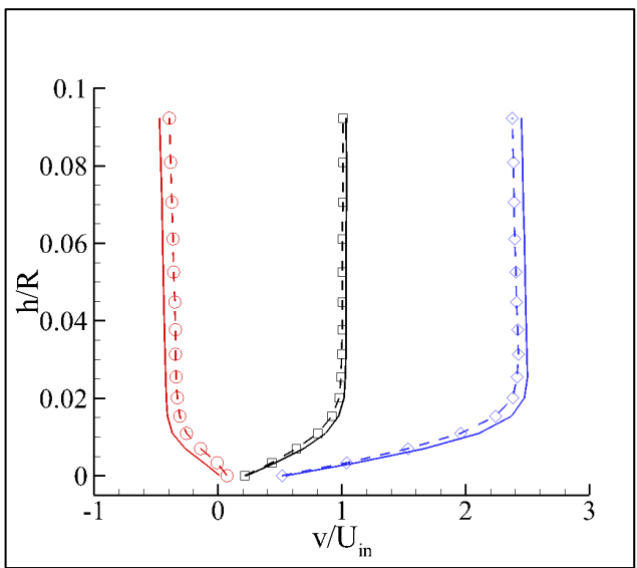
$x/c = 82\%$, $y/R = 73\%$, pressure side



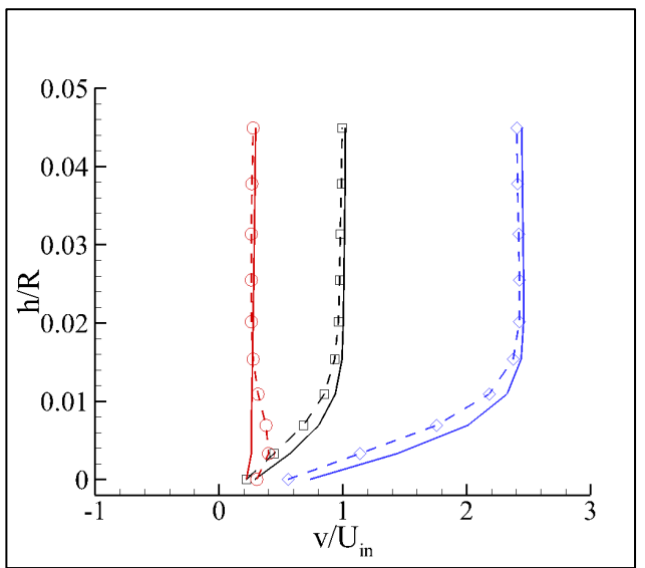
$x/c = 25\%$, $y/R = 90\%$, suction side



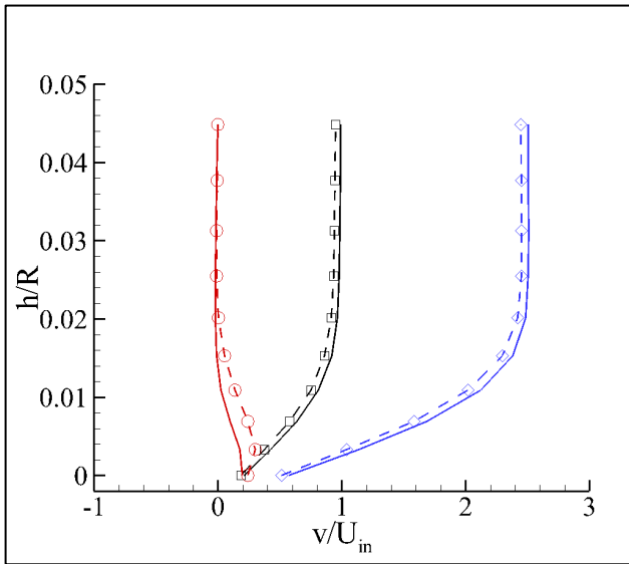
$x/c = 50\%$, $y/R = 90\%$, suction side



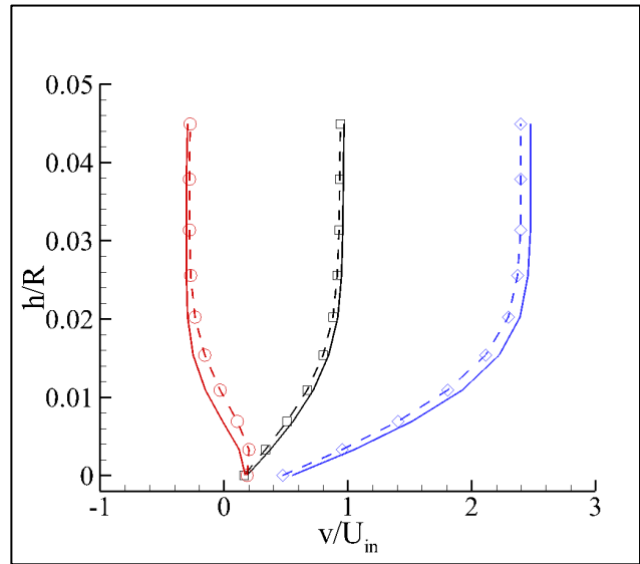
$x/c = 75\%$, $y/R = 90\%$, suction side



$x/c = 25\%$, $y/R = 90\%$, pressure side

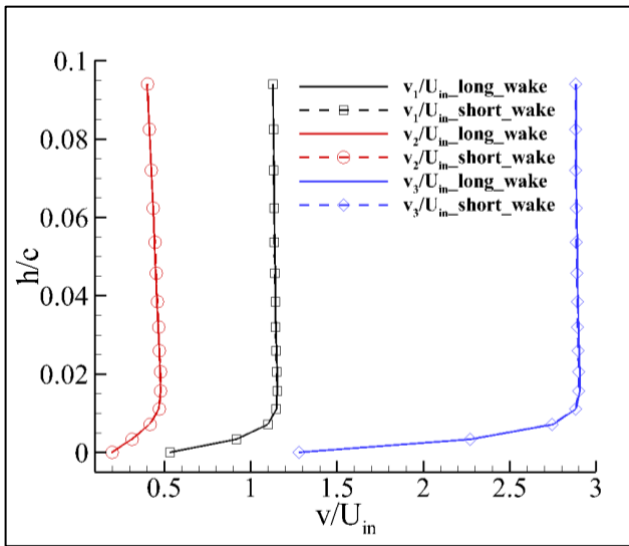


$x/c = 50\%$, $y/R = 90\%$, pressure side

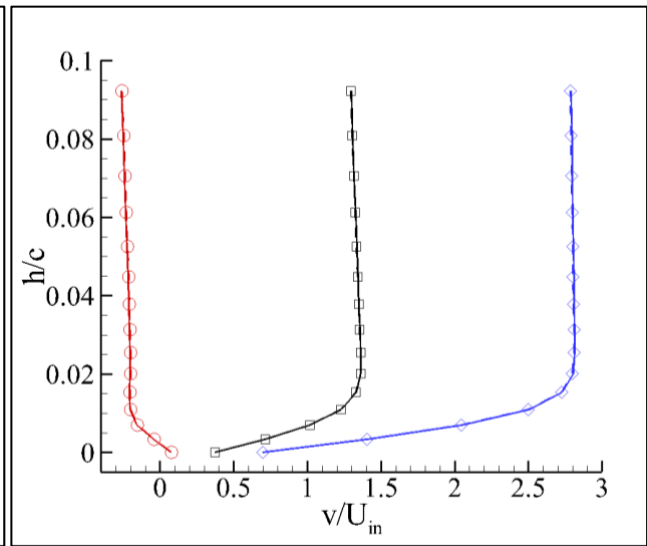


$x/c = 75\%$, $y/R = 90\%$, pressure side

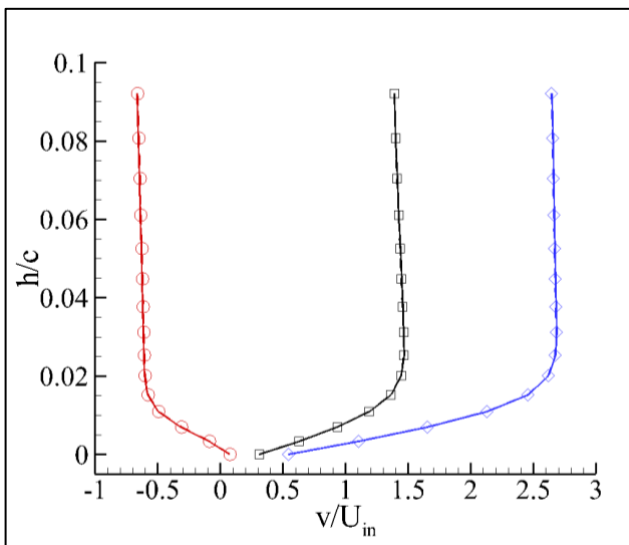
Figure 15 Boundary layer profiles of the propeller at Reynolds number $Re = 5000$ and advance ratio $J = 1.2$



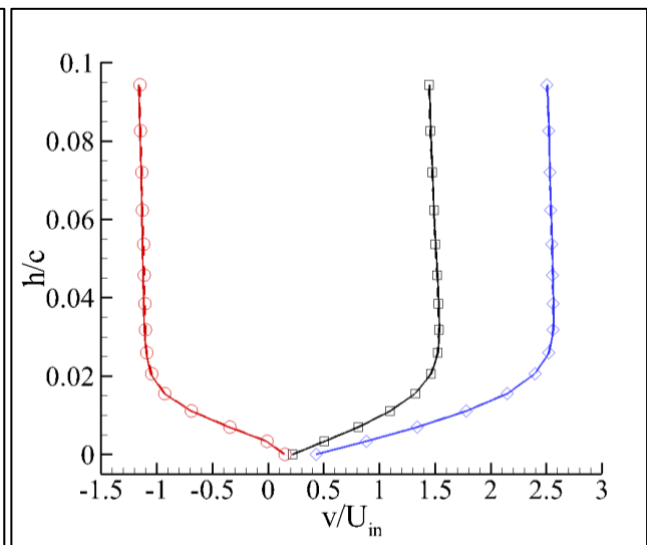
$x/c = 18\%$, $y/R = 73\%$, suction side



$x/c = 43\%$, $y/R = 71\%$, suction side



$x/c = 60\%$, $y/R = 71\%$, suction side



$x/c = 82\%$, $y/R = 73\%$, suction side

Figure 16 The influence of wake length on the results for the proeller case

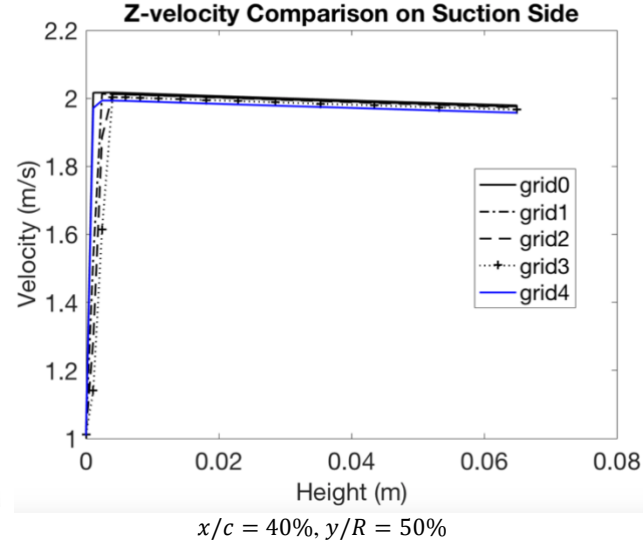
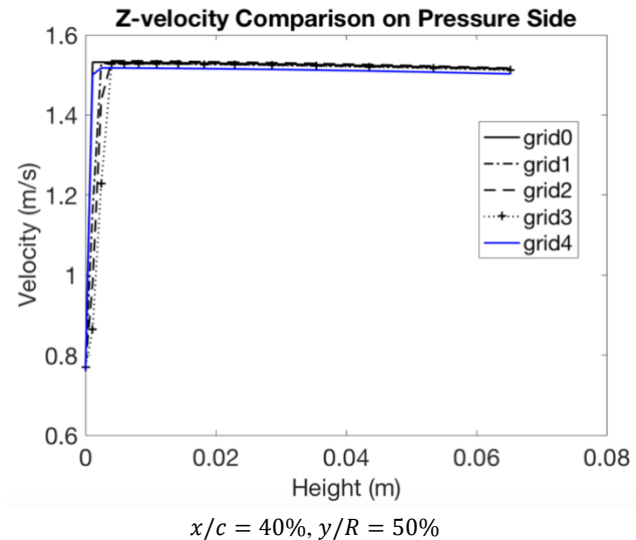
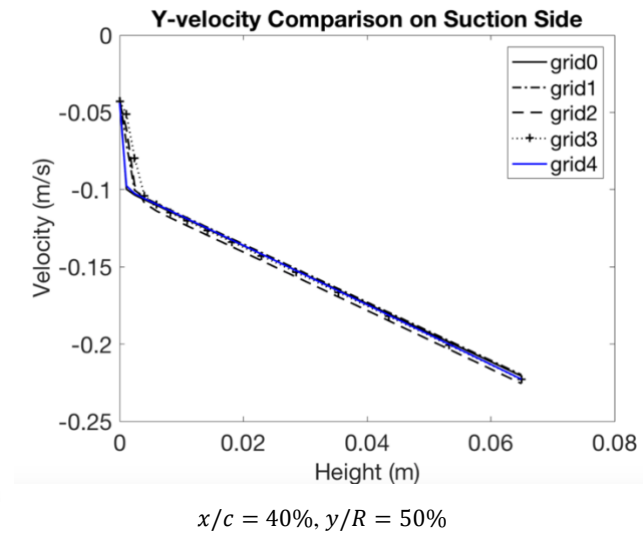
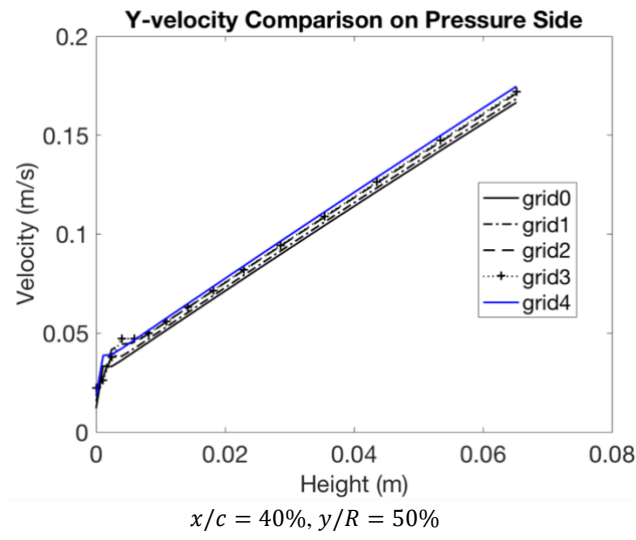
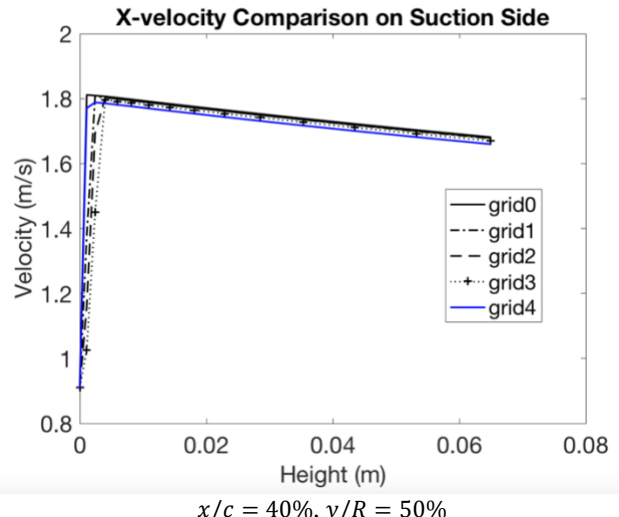
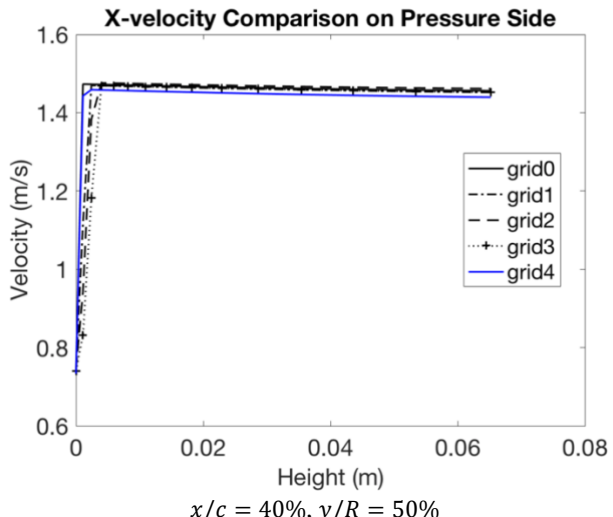


Figure 17 Grid dependence study in the normal direction

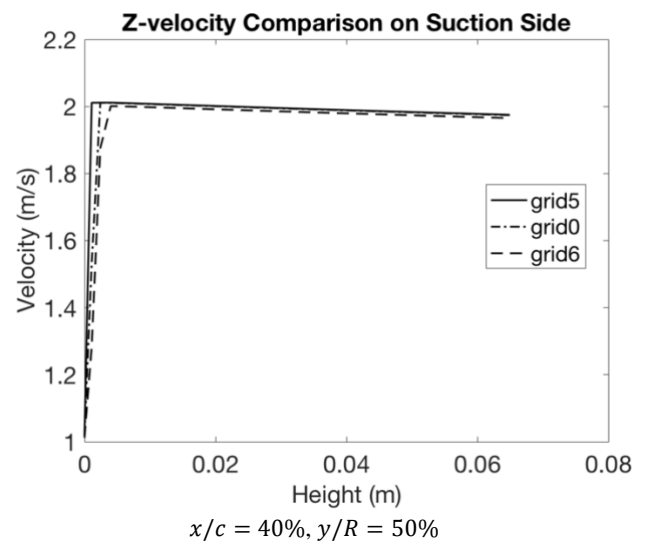
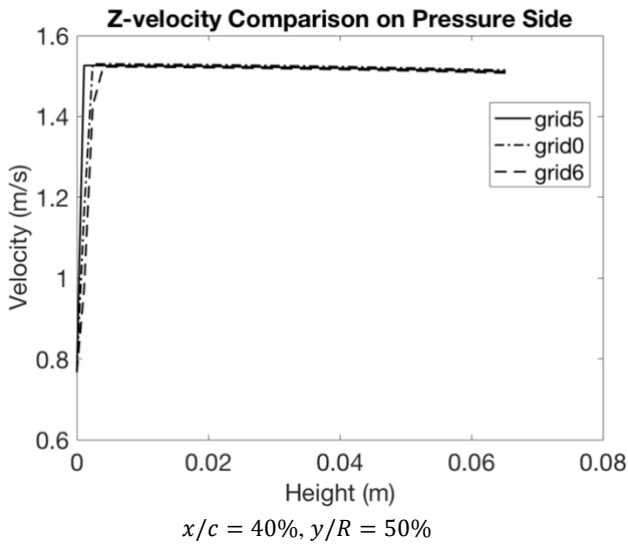
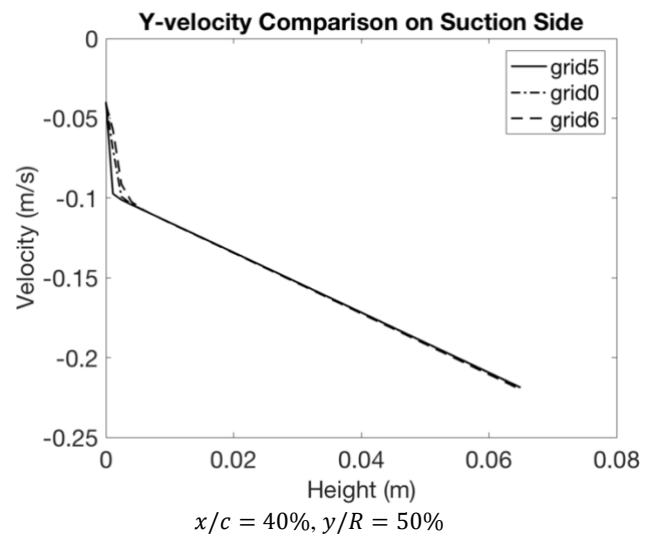
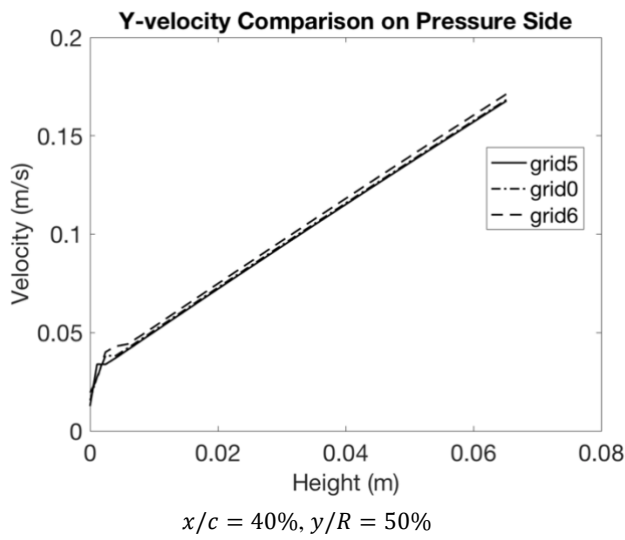
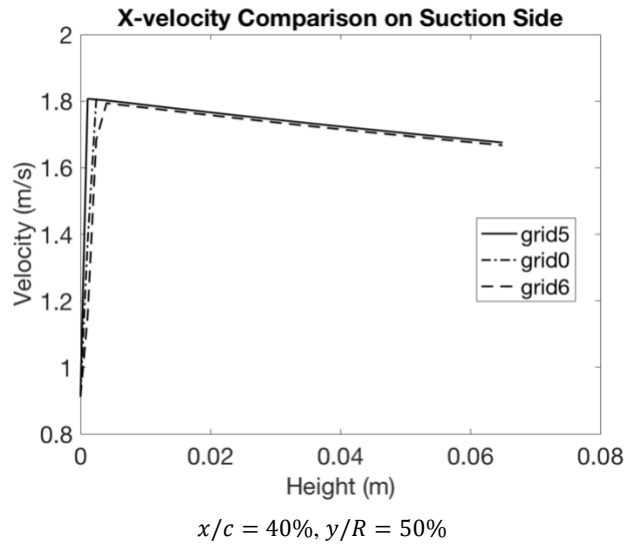
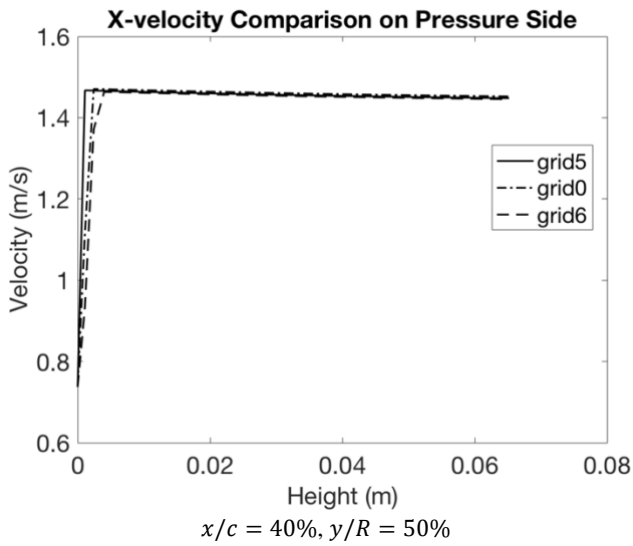


Figure 18 Grid dependence study in the span-wise and chord-wise directions